HIGH TEMPERATURE CHLOROSILANE CORROSION OF IRON AND AISI 316L STAINLESS STEEL

by

Joshua Loren Aller

A dissertation submitted in partial fulfillment
of the requirements for the degree

of

Doctor of Philosophy

in

Mechanical Engineering

MONTANA STATE UNIVERSITY
Bozeman, Montana

November 2016

ACKNOWLEDGEMENTS

First I would like to thank my adviser, Dr. Paul Gannon, and my committee, Dr. Stephen Sofie, Dr. Rob Walker, and Dr. Roberta Amendola for their assistance and guidance on this topic. I'd like to acknowledge Dr. Nathan Jacobson from the NASA Glenn Research Center for performing the thermochemical calculations and being a primary contributor on this project. Also, I would like to acknowledge GT Advanced Technologies for the primary funding and industrial guidance, and the Montana State University College of Engineering for secondary funding. Additionally, I would like to acknowledge the Imaging and Chemical Analysis Laboratory at Montana State University for their help with imaging and sample characterization. I would like to thank the entire High Temperature Materials Laboratory staff for assisting me throughout this work. This includes countless graduate and undergraduate students who assisted with experimental setup, sample preparation, and surface analysis. Finally, I want to thank my wife, Sarah, and my family for their constant support.

TABLE OF CONTENTS

1. INTRODUCTION 1

High Temperature Materials 1
High Temperature Corrosion 2
Parabolic Growth 3
Linear Growth 6
Linear Loss 8
Combinations of Growth Mechanisms 9
Temperature Dependence 12
Chlorosilanes 14
Fumed Silica 14
Semiconductor 15
Silicon Based Photovoltaics 17
Safety Concerns 20
Prior Research 21
Iron 22
Nickel and Chromium 25
Additional Prior Research 25

2. EXPERIMENTAL METHODS 28

Corrosion Exposure 28
Analytical Techniques 31
Field Emission Scanning Electron Microscopy 31
Energy Dispersive X-Ray Spectroscopy 32
X-Ray Diffraction 33
Cross Sectioning and Polishing 34
Gravimetric Analysis 35
Thermodynamic Calculations 37

3. CHLOROSILANE CORROSION OF AISI 316L 41

AISI 316L Introduction 41
AISI 316L Corrosion Exposure Results 42
Composition Dependent Results 42
Temperature Dependent Results 47
Time Dependent Results 50
AISI 316L Corrosion Exposure Conclusions 54

4. CHLOROSILANE CORROSION OF IRON 55

TABLE OF CONTENTS - CONTINUED

Iron Introduction 55
Iron Corrosion Exposure Results 56
Temperature Dependent Results 56
Time Dependent Results 67
Discussion of Iron Chlorosilane Corrosion 74
Conclusions from Iron Chlorosilane Corrosion Study 78

4. INFLUENCE OF SILICON ON THE CHLOROSILANE CORROSION OF IRON 79

Corrosion Environment Introduction 79
Iron Packed Bed Exposure Results 81
Iron Packed Bed Exposure Discussion 91
Iron Packed Bed Conclusions 96

5. GENERAL CONCLUSIONS AND FUTURE WORK 98

6. POSTFACE 102

REFERENCES CITED 104

LIST OF TABLES

Table Page

1. Temperature that common metal-chloride vapor pressures exceed 10^{-4} atm (~10 Pa) 22

2. EDS results for spots labeled in FEM micrographs in Figures 10, 13, and 15 45

3. Equilibrium gas composition calculated by FactSage for several cases relevant for chlorosilane corrosion. 93

LIST OF FIGURES

Figure Page

1. Theoretical mass change plots showing three different corrosion mechanisms 3

2. An example of diffusion-controlled, parabolic growth. In this case, the rate-limiting step is metal diffusion through the corrosion layer to react with the gas to form additional corrosion layer on the surface....4

3. Schematic showing theoretical linear corrosion growth where the gas is allowed immediate access to the metal through open pores or breaks in the corrosion layer. In this case, the reaction of metal and gas is the rate limiting step. 7

4. Example of linear loss corrosion where the gas and metal combine to form a volatile corrosion product. In this case, the reaction of the metal and gas and the subsequent evaporation is the rate limiting step 8

5. Theoretical mass change versus time for a sample growing a parabolic corrosion layer that experiences delamination, cracking, and spallation 11

6. Diagram of a simplified silicon transistor showing the polysilicon gate that is generally deposited using chlorosilanes 16

7. An overview of the silicon manufacturing process beginning with the feedstock of silica (quartz) through to the finished semiconductor or solar panel product. Image copyright of Hemlock Semiconductor 18

8. Schematic of the furnace system used for high-temperature chlorosilane exposures 28

9. Gravimetric analysis from variable HCl testing at 550 and 600°C. The error bars represent a 95% confidence interval 43

LIST OF FIGURES – CONTINUED

Figure Page

10. FEM micrographs and EDS spot scan locations for several AISI 316L samples after exposure to chlorosilane environments with various amounts of HCl at 550°C after 100 hours of exposure. EDS data in Table 2 shows spots 1, 2, and 4 containing primarily Fe and Si and spots 3, 5, 6, and 7 containing significant amounts of Cr and Cl 45

11. Predominance diagram of the Fe-Si-Cl-H system at a.) 550°C and b.) 600°C as generated by FactSage software.....46

12. a.) Area specific gravimetric analysis of 316L after 100 hours at a variety of temperatures in a H_2:STC:HCl environment and b.) transformed gravimetric data used to indicate changes in corrosion mechanism. The error bars represent a 95% confidence interval.....48

13. FEM micrographs of AISI 316L after chlorosilane exposure at a variety of temperatures. EDS results displayed in Table 2 show spots 9 and 10 consistent in composition with 316L and spots 8, 11, 12, and 13 primarily containing Fe and Si.....49

14. a.) Area specific gravimetric analysis and b.) transformed data for time dependent study of chlorosilane corrosion at 700°C. The error bars represent a 95% confidence interval. 51

15. FEM analysis of AISI 316L samples after chlorosilane corrosion at 700°C. EDS results in Table 2 showed all spots containing primarily Fe and Si. Spot 15 also contained significant amounts of Cr and Ni consistent with 316L, indicating a thinner corrosion layer at that point. 52

16. FEM micrographs of cross sectioned 316L sample after chlorosilane exposure. The circle on the lower magnification image indicates the location of the higher magnification image. 53

LIST OF FIGURES – CONTINUED

Figure Page

17. The a) specific mass change data and b) transformed gravimetric data for the temperature dependent study. The transformed data plots the natural log of mass change vs the inverse of absolute temperature. This transformation helps identify changes in corrosion mechanism. A linear trend line for the three higher temperature data points is displayed in b. The error bars represent a 95% confidence interval on the mean.....57

18. The plan view FEM micrographs for the temperature dependent study. These samples were exposed to a STC/H_2 environment for 100 hours at 550, 600, 650, and 700°C.....58

19. The XRD patterns for iron samples after exposure to chlorosilane environments at 550, 600, 650, and 700°C for 100 hours.....59

20. High magnification cross sectional image of a sample after exposure to a chlorosilane environment for 100 hours at 550°C.....60

21. Full width cross sectional image of a sample after exposure to a chlorosilane environment for 100 hours at 600°C. 61

22. Full width cross sectional image of a sample after exposure to a chlorosilane environment for 100 hours at 650°C. The region in the top middle of the image represents remaining, unreacted iron 63

23. High magnification cross sectional image of a sample after exposure to a chlorosilane environment for 100 hours at 700°C. The dark, FeSi on the surface of the sample was seen on all samples exposed at 600°C and higher. 65

LIST OF FIGURES – CONTINUED

Figure Page

24. Thermodynamic modeling showing a.) the predominance diagram for the Iron-Silicon-Chlorine-Hydrogen system at 600°C generated by FactSage and b.) the temperature-composition phase diagram for the iron-silicon system calculated by Kubaschewski and regnerated by Ohnuma. In this diagram, T_c^{α} represents the Currie temperature of the alpha (body centered cubic) phase, B2 represents the Cesium Chloride structure of FeSi, and $D0_3$ represents the cubic structure of Fe_3Si.....66

25. The a) area specific mass change data and b) transformed gravimetric data for the time dependent study. The transformed data plots mass change vs the square root of time to identify if parabolic kinetics are present. The error bars represent a 95% confidence interval on the mean. 68

26. The plan view FEM micrographs for the time dependent study. These samples were exposed to a STC/H2 environment for 8, 24, 48, and 100 hours at 600°C.....69

27. The XRD patterns for iron samples after exposure to chlorosilane environments at 600°C for 8, 24, 48, and 100 hours.....70

28. High magnification cross sectional image of a sample after exposure to a chlorosilane environment for 8 hours at 600°C.....71

29. High magnification cross sectional image of a sample after exposure to a chlorosilane environment for 24 hours at 600°C.....72

30. High magnification cross sectional image of a sample after exposure to a chlorosilane environment for 100 hours at 600°C.....73

31. Proposed corrosion behavior of iron in chlorosilane environments between 600 and 700°C. 75

32. Cross sectional diagram showing the layout of the tube furnace used for chlorosilane exposure and the terminology used to describe the location of samples 80

LIST OF FIGURES – CONTINUED

Figure Page

33. The specific mass change plotted against a.) time and b.) square root of time for samples ● in pack; ▲ out of pack; ◆ no pack; ■ reducing diffusion. Where present, the error bars represent a 95% confidence interval on the mean.. 82

34. Plan view FEM images of "in pack" samples exposed for a variety of times at 600°C 83

35. Plan view FEM images of "out of pack" samples exposed for a variety of times at 600°C 83

36. XRD patterns of a.) "in pack" and b.) "out of pack" samples after a variety of times at 600°C exposures. Peaks are labeled according to identification with Jade software 84

37. Full width cross section and EDS line scan of "in pack" sample exposed for 100 hours at 600°C.....85

38. High magnification image and EDS line scan of "in pack" sample exposed for 100 hours at 600°C 86

39. Full width cross section and EDS line scan of "out of pack" sample exposed for 100 hours at 600°C 87

40. High magnification image and EDS line scan of "out of pack" sample exposed for 100 hours at 600°C 88

41. FEM image and EDS line scan of "in pack" sample exposed for 8 hours at 600°C.....89

42. High magnification image and EDS line scan of "in pack" sample exposed for 8 hours at 600°C 90

43. High magnification image and EDS line scan of "out of pack" sample exposed for 8 hours at 600°C 91

44. FEM images of MG-Si as received and after 100 hour exposure at 600°C 94

LIST OF FIGURES – CONTINUED

Figure Page

45. Plot of MG-Si consumed per run time as measured by weighing the MG-Si before and after exposure. The calculated trend line was (MG-Si consumed (gram)) = 0.0522*(Time (hr)) + 0.0692 with an r-squared value of 0.996 95

ABSTRACT

Chlorosilane gas streams are used at high temperatures (>500°C) throughout the semiconductor, polycrystalline silicon, and fumed silica industries, primarily as a way to refine, deposit, and produce silicon and silicon containing materials. The presence of both chlorine and silicon in chlorosilane species creates unique corrosion environments due to the ability of many metals to form both metal-chlorides and metal-silicides, and it is further complicated by the fact that many metal-chlorides are volatile at high-temperatures while metal-silicides are generally stable. To withstand the uniquely corrosive environments, expensive alloys are often utilized, which increases the cost of final products.

This work focuses on the corrosion behavior of iron, the primary component of low-cost alloys, and AISI 316L, a common low-cost stainless steel, in environments representative of industrial processes. The experiments were conducted using a customized high temperature chlorosilane corrosion system that exposed samples to an atmospheric pressure, high temperature, chlorosilane environment with variable input amounts of hydrogen, silicon tetrachloride, and hydrogen chloride plus the option of embedding samples in silicon during the exposure. Pre and post exposure sample analysis including scanning electron microscopy, x-ray diffraction, energy dispersive x-ray spectroscopy, and gravimetric analysis showed the surface corrosion products varied depending on the time, temperature, and environment that the samples were exposed to. Most commonly, a volatile chloride product formed first, followed by a stratified metal silicide layer. The chlorine and silicon activities in the corrosion environment were changed independently and were found to significantly alter the corrosion behavior; a phenomenon supported by computational thermodynamic equilibrium simulations. It was found that in comparable environments, the stainless steel corroded significantly less than the pure iron. This is likely due to the alloying elements present in stainless steel that promote formation of other stable silicides.

Mechanistic models were developed to describe the formation and evolution of metal silicide and/or metal chloride surface corrosion products in chlorosilane environments. These models will help inform materials selection and/or support process development for next-generation chlorosilane-based production and deposition systems. The implementation of low cost materials of construction in these systems could lower the cost of final products in these industries.

INTRODUCTION

High Temperature Materials

Materials have historically been a defining factor for civilizations. Technological progress is so dependent on the ability to create and shape materials that often times generations are named after their primary material discoveries, e.g. Bronze Age and Stone Age [1]. Currently, there is a push in science and engineering to create materials that can withstand higher and higher temperatures for use in energy conversion, chemical processing, and aerospace applications [2].

Materials at high temperature are generally limited by either their mechanical properties such as strength and stiffness or chemical properties such as reactivity with the application environment. Failures due to loss of strength and stiffness are generally due to the high temperature creep of the material. It is well known that materials soften at high temperatures and begin to exhibit viscoelastic behavior [3]. This causes the material to deform over time and potentially break. Failures due to material reactivity are often referred to as corrosion failures [1]. Corrosion failures are generally caused by the atmosphere reacting with the structural material. The new material formed by this reaction generally has less desirable mechanical properties than the starting material. If this change in properties is not accounted for, it can lead to material failure. This failure mechanism in a unique chlorosilane environment will be the primary focus of this dissertation.

There are many applications that are limited by the high temperature corrosion behavior of structural materials. These include aircraft engines, chemical reactors, and steam turbines [4-6]. In many of these applications, increased operating temperature increases the efficiency of the system. However, it also decreases the longevity of the material. Therefore, the efficiency of the turbine, reactor, or engine is limited by the materials of construction. In today's energy conscience society, it is imperative to maximize energy and material efficiencies. To improve efficiencies, higher temperature materials must be developed to withstand these environments.

High Temperature Corrosion

Before discussing high temperature corrosion in a chlorosilane environment, it is important to consult the theory behind other forms of high temperature corrosion that are better understood. The most common high temperature corrosion environment is an oxidizing environment and there is a substantial amount of information available regarding metal oxide formation. Oxidizing environments are generally the result of hydrocarbon combustion or high temperature steam used in turbines [4-6]. The presence of oxygen at high temperatures in both cases can cause metals to form metal oxides. In some cases, these metal oxides are thin and protective. This is the case with chromium oxide formation in stainless steel at room temperature [1]. The chromium oxide protects the rest of the metal from further oxidation and allows the base metal to maintain its mechanical properties. In other cases, the metal oxide is not protective. One example of a non-protective metal oxide is rust or iron oxide. Rust forms on unprotected iron and steel components that are exposed to oxygen [1]. When it forms, it can flake off or

disintegrate, exposing additional iron that can be oxidized. This cycle consumes the base metal and given enough time, will result in component failure. The causes of protective and non-protective corrosion scale formation will be discussed in further detail here in context of understanding the mechanisms of metal oxide surface layer formation. The oxide formation mechanism dictates the surface layer growth kinetics, interfacial strength, and stratification that may occur. The most common models of growth kinetics include parabolic, linear growth, and linear loss [7]. Theoretical mass change as a function of time for each model is shown in Figure 1. Each will be discussed briefly here.

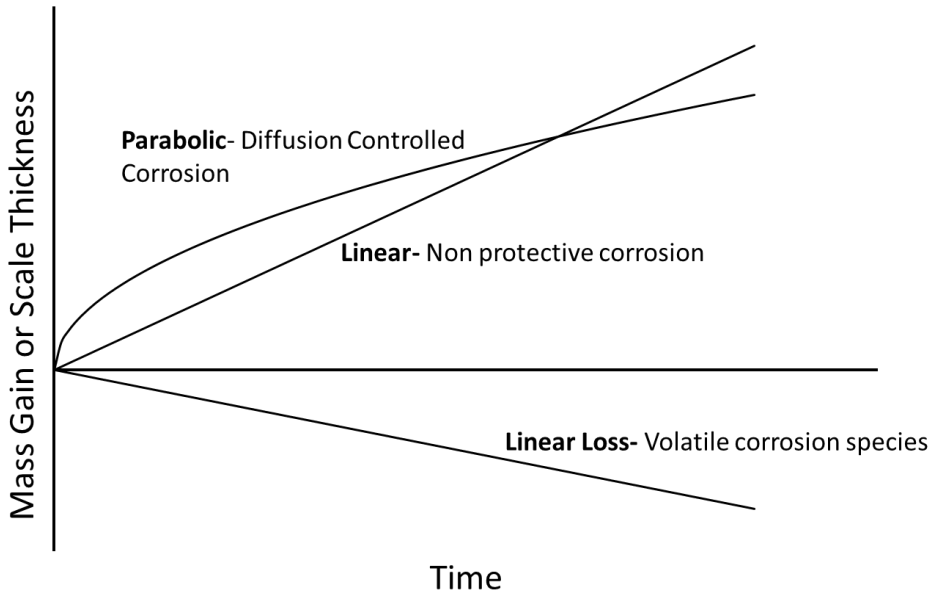

Figure 1: Theoretical mass change plots showing three different corrosion mechanisms.

Parabolic Growth. In general, an engineer would prefer an alloy that exhibits parabolic behavior over many other form of corrosion [7]. In order to have parabolic growth, there must be a base metal, a continuous corrosion layer, and a reacting gas as shown in Figure 2; adapted from Young [5]. For parabolic kinetics, the corrosion layer

must be protective and continuous meaning that is does not provide a direct path for the gas to access the base metal. In this case, either metal or gas ions must diffuse through the corrosion layer to react and form a thicker corrosion layer. For parabolic growth, the diffusion of the metal or gas ions through the corrosion layer must be the limiting step in corrosion layer growth [4-8]. Figure 2 also shows the dissociation reactions of the corrosive gas and metal, which are necessary for corrosion layer growth, but not rate limiting in parabolic kinetics.

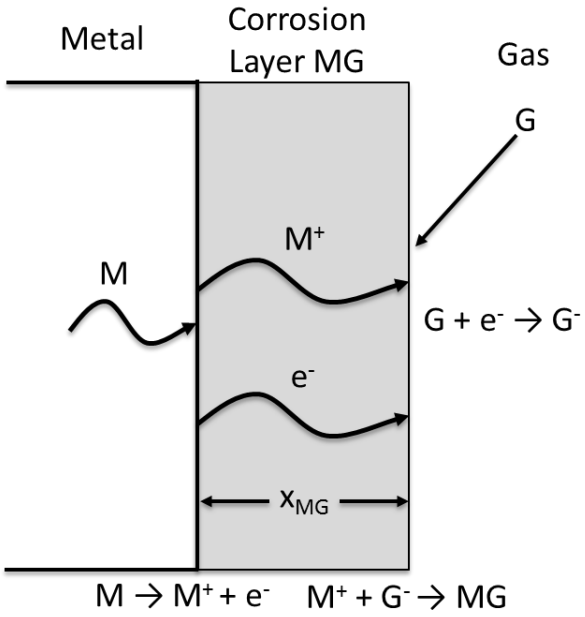

Figure 2: An example of diffusion-controlled, parabolic growth. In this case, the rate-limiting step is metal diffusion through the corrosion layer to react with the gas to form additional corrosion layer on the surface.

Knowing that the corrosion layer growth is diffusion controlled, a few equations can be written to formalize the relationship. This derivation is based on the Wagner theory of oxidation, and follows the derivation by Birks, et al [9]. In this example, the assumption is made that the metal is the primary diffusing species and its reaction with

the gas atmosphere is not the limiting step. Equation 1 represents Fick's First Law showing that the flux of metal, J_M, is equal to the diffusion coefficient, D_M, multiplied by the chemical potential gradient shown here as the difference in species concentration divided by layer thickness, $\Delta C_M/x_{MG}$. Equation 2 is the definition of molar flux, showing that the flux of the metal is equal to the molar density of the diffusing species, $1/v_M$, multiplied by the layer thickening rate, dx_{MG}/dt. These two equations can be set equal to each other, and the differential equation can be solved using a separation of variables technique. Assuming an initial scale thickness of zero and constant temperature and concentration gradient, it can be simplified to Equation 3 where the scale thickness, x_{MG}, squared is equal to a constant, k_p, multiplied by time, t. This relationship results in a shape represented by Figure 1 where the rate of scale thickness growth decreases with time.

$$J_M = -D_M \frac{\Delta C_M}{x_{MG}} \tag{1}$$

$$J_M = \frac{1}{v_M} \frac{dx_{MG}}{dt} \tag{2}$$

$$x_{MG}^2 = k_p t \tag{3}$$

While this situation represents ideal parabolic growth, there are some assumptions that were made that may not always be true. The first assumption is that the concentration gradient and diffusivity are not functions of exposure time or corrosion layer thickness. Also for parabolic growth, there must be a continuous corrosion layer established that limits the formation of a thicker layer. Generally, it takes some amount of time for this layer to form, meaning that parabolic kinetics do not begin until sometime after the corrosive exposure has begun. Another assumption is that the corrosion layer can grow to

infinite thickness. This is not generally true due to stresses that build up as the layers grow thicker. When the scale stress exceeds the interfacial strength, it can flake off of the base metal, exposing new metal to be corroded. This will start the parabolic-relation over again. Another assumption of the parabolic rate law is that there is only one corrosion product. In a pure oxidizing environment with one metal, this may be the case. However, often times both the environment and the metal are more complex than that, causing there to be variations from the parabolic rate law. Furthermore, the impact of grain boundaries on diffusivity may cause the corrosion mechanisms to deviate from pure parabolic kinetics. It is well known that diffusion in grain boundaries is often times faster than bulk diffusion through a crystal. Therefore, the number of grain boundaries will likely change the diffusivity. If the corrosion scale can undergo grain growth or grain reduction as it forms, it will likely change the diffusivity, causing the scale growth to no longer follow parabolic kinetics. Due to these and other assumptions, it cannot be reasonably expected that perfect parabolic kinetics will exist, even in diffusion controlled corrosion. However, it is a good model to compare against, and is generally considered a best case scenario.

Linear Growth. Linear growth is the process of uninhibited surface corrosion scale growth that does not slow over time. This type of corrosion scale formation occurs when there is a continuous supply of base metal and gas available to react [7]. A common example of this would be a porous or discontinuous scale as shown in Figure 3. A porous scale allows the gas access to the metal where it can react to form a corrosion product. Therefore, the reaction takes place at a metal-gas interface rather than a metal-corrosion product interface or corrosion product-gas interface.

Other situations that cause linear growth kinetics include reaction-limited corrosion and nucleation-limited corrosion. An example of reaction limited corrosion is displayed in Figure 2, except now the rate limiting step is no longer the diffusion of species through the corrosion layer, rather it is the reaction of the species at the interfaces. This requires sufficiently fast species diffusion and/or slow reaction rates. In all of these cases, a continuous, protective scale does not form to inhibit further corrosion. Linear growth corrosion is generally problematic in industrial situations because the scale growth theoretically continues at a constant rate which can compromise the base metal structural integrity and/or its process function.

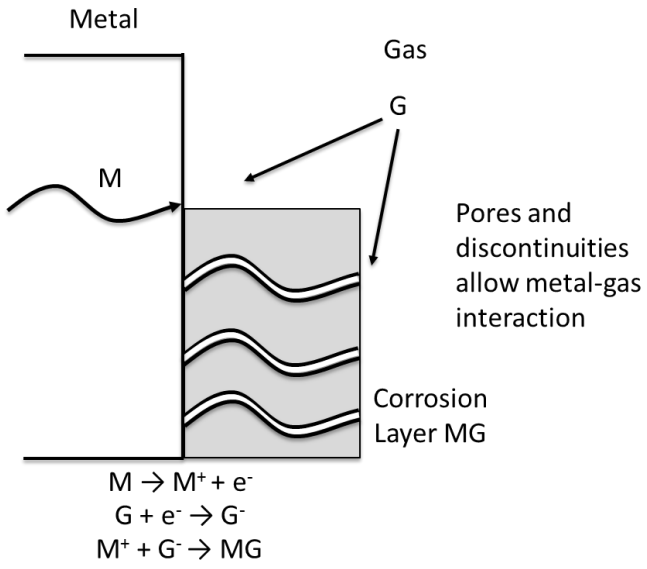

Figure 3: Schematic showing theoretical linear corrosion growth where the gas is allowed immediate access to the metal through open pores or breaks in the corrosion layer. In this case, the reaction of metal and gas is the rate limiting step.

Linear Loss. Linear loss kinetics is the loss of base material as a result of corrosion. This type of corrosion generally occurs when the corrosion product is volatile

in the exposure environment [8]. The most common type of linear loss corrosion is known as reactive evaporation. This occurs when the metal and gas combine to form a product with a sufficiently high vapor pressure that evaporates in to the gas stream. An example of linear loss corrosion is displayed in Figure 4, which shows metal, M, combining with gas, G, to form a vapor MG, which consumes base metal. Linear loss kinetics are generally a worst case scenario because the structural material is essentially being uncontrollably dissolved into the corrosive environment, reducing the amount of structural material available to carry a load.

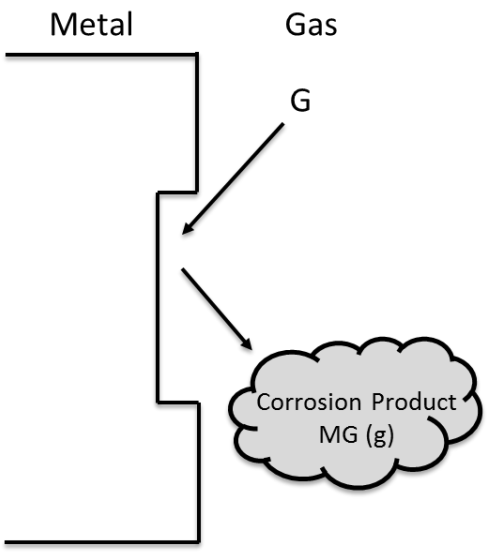

Figure 4: Example of linear loss corrosion where the gas and metal combine to form a volatile corrosion product. In this case, the reaction of the metal and gas and the subsequent evaporation is the rate limiting step.

Combinations of Growth Mechanisms. While parabolic, linear growth, and linear loss kinetics can all be readily explained theoretically, actual corrosion scales generally

grow as a combination of several mechanisms. A few examples of mixed kinetics will be described here.

The first example is called paralinear growth. In paralinear growth, the corrosion process is initially nucleation-limited meaning the corrosion product initially forms at points on the sample. These points then grow in to larger areas which generally results in a linear process. Eventually, the areas grow together forming a continuous scale. Once the continuous scale has formed, there is potential for continued growth to be diffusion controlled, resulting in parabolic growth.

Another growth mechanism is the combination of parabolic and linear loss kinetics. This mechanism is often the result of forming several corrosion products with drastically different properties. One example of this situation is a metal, M, interacting with a mixed gas, X and G. In this scenario, MG is a protective surface layer and MX is a volatile corrosion product. The formation of MG and MX by several different reactions is shown in Equations 4-6. MG formation modeled by Equation 4 would result in parabolic kinetics because it is a protective surface layer. MX formation modeled by Equation 5 would result in linear loss kinetics due to the formation of a volatile corrosion product. However, this formation of the volatile corrosion product would no longer happen after a stable MG layer had formed unless the reaction modeled by Equation 6 occurs. If it does occur, parabolic growth from Equation 4 and linear loss from Equation 6 are additive making this a combinatorial growth mechanism. If Equation 6 does not occur, then only long term parabolic kinetics from MG formation should be expected with some short

term linear loss from Equation 5. This situation demonstrates that simple models do not always apply to real situations, and they must be modified accordingly.

$$M(s) + G(g) \rightarrow MG(s) \quad (4)$$

$$M(s) + X(g) \rightarrow MX(g) \quad (5)$$

$$MG(s) + X(g) \rightarrow MX(g) + G(g) \quad (6)$$

Spallation and scale cracking also influence corrosion rate [6]. An example of this is shown in Figure 5; adapted from Birks, et al [9]. This figure shows an idealized parabolic growth curve with some interruptions that may occur. The first interruption is separation of the metal and corrosion scale. This separation limits transport of the reacting metal or gas which slows the corrosion rate. Eventually this separation leads to a crack in the corrosion scale. Once this crack forms, it allows the gas to access the metal and continue growing the scale. The scale continues to grow thicker until it builds up enough stress that it results in spallation. This results in a significant mass loss as shown in Figure 5. However, it also reduces the scale thickness which causes increased mass gain. These unpredictable changes in corrosion scale thickness and corrosion rate further complicate the realities of corrosion scale formation.

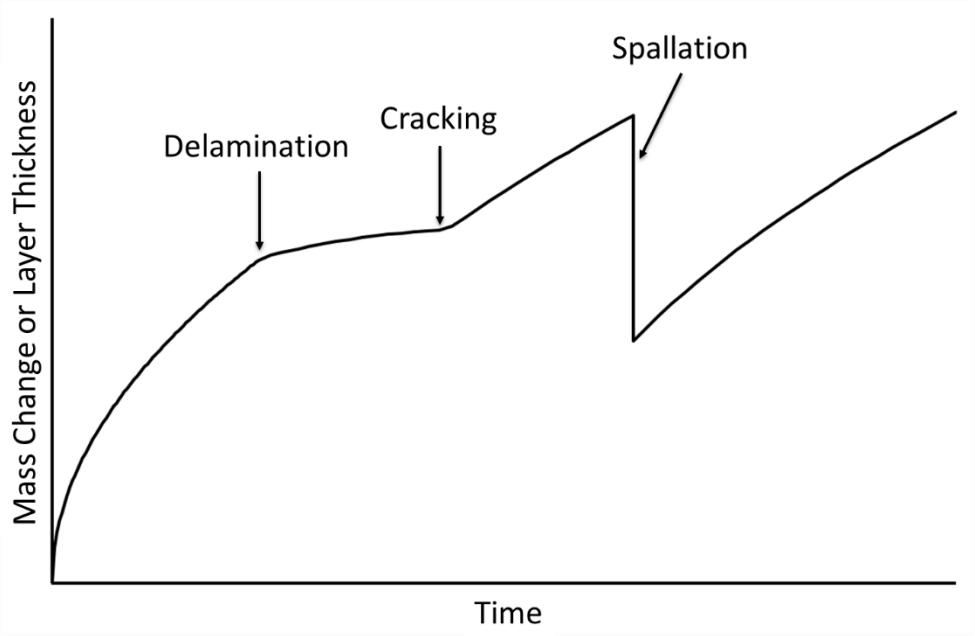

Figure 5: Theoretical mass change versus time for a sample growing a parabolic corrosion layer that experiences delamination, cracking, and spallation.

Another phenomena that occurs in highly corrosive environments is breakaway corrosion. Breakaway corrosion is common in alloys that form a generally protective scale through the reaction of an alloying element with the corrosion environment. This scale formation lowers the concentration of that alloying element in the remainder of the substrate. This depletion leaves the rest of the substrate vulnerable to attack when the protective scale cracks from spallation or other means. Breakaway corrosion is often unpredictable and its occurrence can be catastrophic.

Even though the majority of these growth mechanisms were developed for oxidizing environments, they can also occur in other corrosive environments. In the remainder of this document, comparisons will be drawn between oxidation kinetics and kinetics present in chlorosilane environments. This allows for application of generalized corrosion theory to a unique environment.

Temperature Dependence. The previous discussion primarily involves the kinetics of corrosion layer growth, particularly the theoretical dependence of corrosion layer thickness on time. This discussion will focus on the influence of temperature on corrosion mechanisms. The primary corrosion mechanisms of interest are diffusion-limited corrosion and reaction-limited corrosion. Because both diffusion and reaction are thermally activated processes, they will typically have an exponential relationship with temperature. In the case of diffusion-limited corrosion, the mass change, Δm, will be proportional to the species flux, J, through the corrosion layer as shown in Equation 7 [7]. The flux, according to Fick's first law (Equation 8), is equal to the negative diffusion coefficient, D, times the chemical potential gradient shown here as the concentration gradient, dc/dx. The diffusion coefficient is equal to a constant, D_o, multiplied by the exponential of the negative activation energy of diffusion, E_{AD}, divided by Boltzmann's constant, k, multiplied by absolute temperature, T, as shown in Equation 9. Taking the natural log of both sides and substituting for mass gain yields the relationship shown in Equation 10.

$$\Delta m \propto J \tag{7}$$

$$J = -D\frac{dc}{dx} \tag{8}$$

$$D = D_0 e^{-E_{AD}/k*T} \tag{9}$$

$$\ln(\Delta m) \propto (\ln(D_0) - E_{AD}/k * T) \tag{10}$$

In the case of reaction rate limited corrosion, the mass change is proportional to the rate of the reaction as shown in Equation 11. The reaction rate is equal to the reaction rate coefficient, K(T), multiplied by the concentration of the reactants ($[M^+]$, $[G^-]$) raised

to a power (m, n) as shown in Equation 12. The reaction rate coefficient is defined by Equation 13 and is very similar in structure to Equation 9, except here the applicable activation energy is that of the reaction, E_{AR}. Taking the natural log of both sides reveals the relationship shown in Equation 14, which is very similar to Equation 10.

$$\Delta m \propto r \tag{11}$$

$$r = K(T) * [M^+]^m * [G^-]^n \tag{12}$$

$$K(T) = Ae^{-E_{AR}/k*T} \tag{13}$$

$$\ln(\Delta m) \propto (\ln(A) - E_{AR}/k * T) \tag{14}$$

These equations hold a significant amount of power in the fact that the natural log of mass change can be plotted against the inverse of absolute temperature, with the slope of the line being the activation energy of the limiting step divided by the negative of Boltzmann's constant. Therefore, a change in slope represents a change in activation energy, and likely a change in corrosion mechanism. This relationship is shown in Equations 15 and 16. This relationship will primarily be used in this work to show changes in predominate corrosion mechanism as a function of temperature. For example, a corrosion layer's formation may be reaction-limited at low temperature and diffusion-limited at high temperature. If this is the case, the plot of inverse temperature versus natural log of mass change will result in two lines of differing slopes.

$$\ln(\Delta m) \propto \frac{1}{T}c + b \tag{15}$$

$$c \propto -E_A \tag{16}$$

It should be noted in these equations that the gas constant, R, can be used in place of the Boltzmann's constant, k, with the difference being a multiplication by Avogadro's

number. In general, Boltzmann's constant is used in conjunction with pure particle counts while the universal gas constant is used in conjunction with molar amounts. The implications are the same regardless of the constant. This dissertation uses Boltzmann's constant due to its use in references [9].

Chlorosilanes

Chlorosilanes in general are compounds that contain silicon, chlorine, and/or hydrogen. The most common species in a chlorosilane mixture are silicon tetrachloride (STC, $SiCl_4$), trichlorosilane (TCS, $HSiCl_3$), dichlorosilane (DCS, H_2SiCl_2), and silane (SiH_4). In industry, they are generally combined with hydrogen (H_2) as a carrier gas and hydrogen chloride (HCl) as a byproduct of processing. It should be noted that the HCl that accompanies chlorosilane species is anhydrous meaning that it is not an aqueous solution. Chlorosilanes are used in many industries for the production of silicon and silicon-containing materials including the fumed silica industry, semiconductor industry, and the solar silicon industry [10-13]. Since 2008 the solar silicon industry has been the largest volume producer and user of chlorosilanes, so the discussion will focus on this application. However, the other industries will be discussed in sufficient detail to provide context for the research. Additionally, the safety concerns associated with handling and disposing of chlorosilanes will be discussed in this section.

Fumed Silica

The fumed silica industry utilizes chlorosilanes, primarily STC, to produce ultra-high purity fumed silica (SiO_2). Fumed silica is a desiccant and binder in products such as

makeup, toothpaste, and paint. It is most commonly produced according to Equation 17 [12]. This equation shows the combination of silicon tetrachloride with hydrogen and oxygen to form silica and hydrogen chloride. This reaction takes place at high temperature (>1500°C) which creates a corrosive environment that must be accounted for.

$$SiCl_4 + 2H_2 + O_2 \rightarrow SiO_2 + 4HCl \quad (17)$$

Additionally, the production of HCl should be noted as a byproduct of the reaction. This will be a common theme when dealing with chlorosilanes and its production only adds to the complexities of handling the gas stream.

Semiconductor

The semiconductor industry requires silicon and silicon species for nearly all of their substrate and deposited materials. The production of the silicon wafer substrate is included in the polysilicon production process which will be discussed later. However, chlorosilanes are used for deposition of many other silicon containing materials [14]. Perhaps the most common example is in a standard MOSFET (Metal Oxide Semiconductor Field Effect Transistor) shown in Figure 6. In this transistor, the source and drain regions are doped portions of the silicon wafer substrate. However, the polysilicon gate is generally deposited using a chemical vapor deposition (CVD) process.

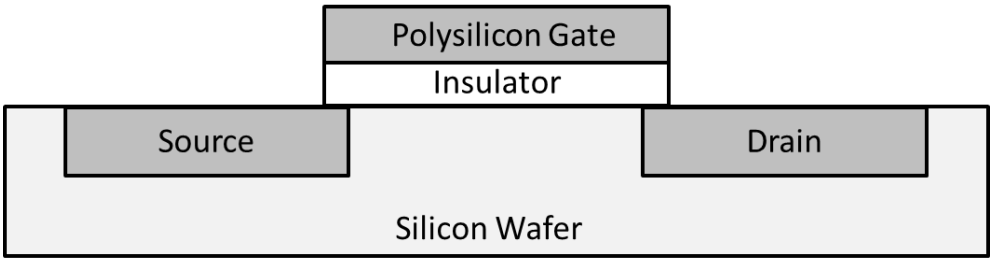

Figure 6. Diagram of a simplified silicon transistor showing the polysilicon gate that is generally deposited using chlorosilanes.

The silicon source for deposition varies, but common choices include silane, DCS, TCS, and STC [14]. Equations 18 - 21 are simplified models of these deposition processes. It should be noted that in reality, each of these reactions are highly complex and multistep, but the simplification allows for easy identification of products and reactants.

$$SiH_4 \rightarrow Si + 2H_2 \quad (18)$$

$$H_2SiCl_2 \rightarrow Si + 2HCl \quad (19)$$

$$HSiCl_3 + H_2 \rightarrow Si + 3HCl \quad (20)$$

$$SiCl_4 + 2H_2 \rightarrow Si + 4HCl \quad (21)$$

Each of these deposition processes require different temperatures and pressures to occur at appreciable rates, but any of them can be used depending on the desired silicon morphology. Additionally, many silicides or silicon containing compounds must be deposited in the semiconductor production process. In many of these deposition process, chlorosilanes are again used as a silicon source to make compounds such as silicon nitride or nickel silicide.

Silicon Based Photovoltaics

As the realities of global climate harms caused by fossil fuel emissions become more apparent, society has turned to renewable energies such as solar. This has resulted in an increase in solar capacity of approximately 40% annually [15]. Silicon based photovoltaic (Si-PV) technology is the leading implementation of directly harnessing solar energy. This increased demand requires a steady supply of silicon to be used as a feedstock for Si-PV substrates. While silicon is the second most abundant element in the earth's crust, it is primarily bonded to oxygen in the form of SiO_2 or quartz. Before being used in a Si-PV panel, it must be reduced to a metal, purified, deposited, and grown into the desired crystalline form.

An overview of the silicon industry is shown in Figure 7. This shows the overall process of how silicon goes from an oxide to an ultrapure metal to be used in solar, electronic, or other applications. The first step of this process is to reduce silica (SiO_2) into silicon (Si) using a carbon arc furnace. At this point, some physical purification techniques are employed to reach a silicon purity level of approximately 98% which is known as metallurgical grade silicon. This metallurgical grade silicon is then reacted with hydrogen and chlorine containing gases at high temperatures to make chlorosilanes. These chlorosilanes are then purified to part per trillion purity levels, primarily through the use of distillation columns. After purification, the chlorosilanes are introduced into a chemical vapor deposition system at high temperatures where they decompose into ultra-high purity polycrystalline silicon (polysilicon) that can be used as a feedstock for solar cell and semiconductor manufacturing. This silicon is typically on the order of 1 part per

billion (ppb) impurity, meaning that counting atoms at a rate of 1 per second, only 1 non-silicon atom would be found every 32 years. For comparison, 1 percent impurity would correspond to finding a non-silicon atom every 100 seconds.

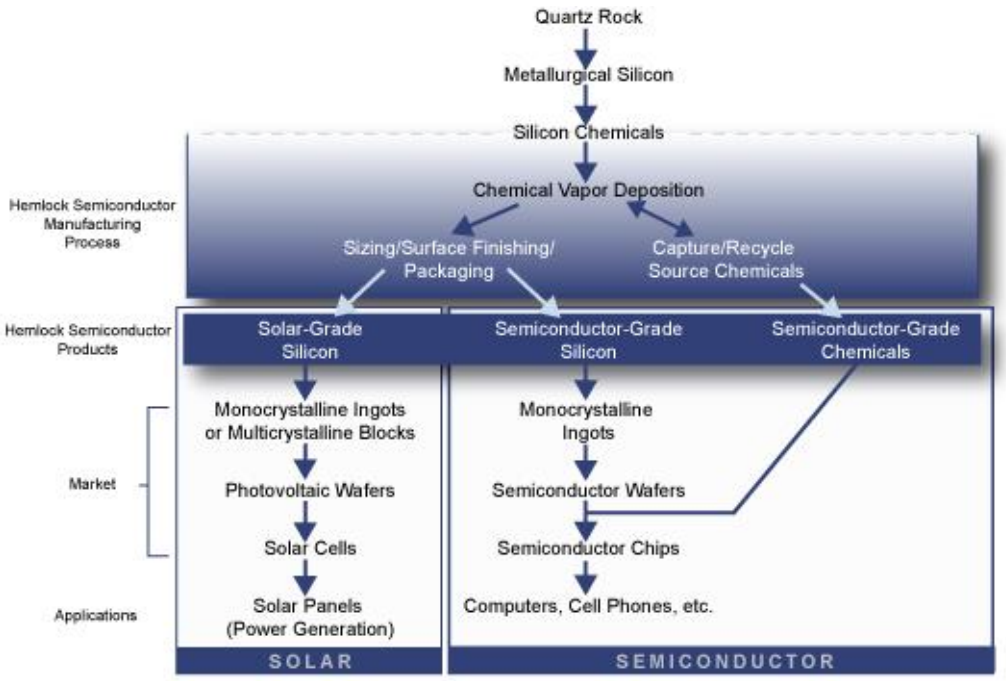

Figure 7. An overview of the silicon manufacturing process beginning with the feedstock of silica (quartz) through to the finished semiconductor or solar panel product. Image copyright of Hemlock Semiconductor.

There are several important reactions in the polysilicon production process. The first is the hydrochlorination of silicon to form trichlorosilane [16-18]. This reaction typically takes place in a fluidized bed reactor with small particles of metallurgical grade silicon. The overall reaction is shown in Equation 22. Many authors have investigated this reaction and found that it is multistep and includes some side reactions that produce other species including HCl and DCS [10, 17, 19].

$$3SiCl_4 + 2H_2 + Si \rightarrow 4HSiCl_3 \quad (22)$$

Another critical reaction to understand in the production of polycrystalline silicon is the chemical vapor deposition of silicon via TCS [11]. The first step in this process has been previously discussed in Equation 20. However, this reaction produces HCl which also reacts with TCS to form STC. This reaction is shown in Equation 23 with the overall CVD reaction shown in Equation 24.

$$HSiCl_3 + HCl \rightarrow H_2 + SiCl_4 \quad (23)$$

$$2HSiCl_3 \rightarrow Si + SiCl_4 + 2HCl \quad (24)$$

The complexity of the silicon-hydrogen-chlorine system is apparent when evaluating these equations, but the point is that chlorosilanes are often converted via reaction with HCl or H_2 and TCS is generally the preferred chlorosilane for CVD processes. However, the safety concerns associated with TCS (discussed later) and the production of STC from the CVD of TCS make STC the preferred chlorosilane for storage and handling.

The polycrystalline silicon industry requires large, sophisticated gas handling equipment, process vessels, and reactors to produce and handle the chlorosilanes necessary for ultrapure silicon production. Many of the reactions described previously take place at high temperatures necessitating the use of expensive, corrosion resistant alloys to construct the reactors and vessels [17]. The use of these expensive metals to resist chlorosilane attack significantly contributes to the capital equipment cost associated with a polycrystalline silicon production plant. In fact, the depreciation and interest associated with capital equipment contributes to approximately half the cost of a kilogram of polysilicon [16]. Additionally, polysilicon production is by far the most

capital intensive step in making and installing solar panels [20]. The high capital equipment cost is partially due to the size of the plants required to make and purify silicon. However, it is also due to the high cost alloys that are generally employed to increase chlorosilane corrosion resistance. If low cost alloys could be used, it would greatly decrease the capital equipment cost associated with polysilicon, making solar energy more cost competitive with traditional fossil fuels.

Safety Concerns

When handling chlorosilanes, it is crucial to keep safety a high priority. Each chlorosilane has slightly different safety criteria, but in general they should be handled in an inert environment and the exposure to air, water, and water vapor should be minimized. This is due to many chlorosilanes being pyrophoric meaning that they react spontaneously when they come in to contact with the water vapor in air. The oxidation is multistep and complex, but it can simply be modeled for DCS in Equation 25, TCS in Equation 26, and STC in Equation 27.

$$H_2SiCl_2 + 2H_2O \rightarrow SiO_2 + 2H_2 + 2HCl \quad (25)$$

$$HSiCl_3 + 2H_2O \rightarrow SiO_2 + H_2 + 3HCl \quad (26)$$

$$SiCl_4 + 2H_2O \rightarrow SiO_2 + 4HCl \quad (27)$$

In each case, the chlorosilane primarily reacts with the water vapor in the air rather than oxygen. For DCS and TCS, the reaction products are silica (SiO_2), hydrogen chloride, and hydrogen, with DCS producing twice as much hydrogen as TCS. The silica is relatively inert and the primary possible health risk is silicosis depending on the particle size and shape. However, the hydrogen and hydrogen chloride both pose

immediate, serious health risks. Hydrogen is very flammable, and both of these reactions are sufficiently exothermic to ignite the evolved hydrogen. Hydrogen chloride is also poor for human health and can cause serious airway issues. STC does not produce hydrogen, making it non-pyrophoric, and safer overall. Because of the increased safety, STC is generally the preferred form of chlorosilane for storage and laboratory use. The pyrophoric nature of chlorosilanes also complicates their disposal. They must be fully oxidized prior to disposal to prevent them from oxidizing and producing hydrogen unexpectedly. This must be done in a controlled manner to prevent the evolved hydrogen from igniting.

Prior Research

Chlorosilane species create unique corrosion environments for the metallic materials tasked with handling chlorosilane gas streams due to the ability of many metals to form both metal-silicides and metal-chlorides. Metal-silicide and metal-chloride formation has been studied extensively primarily for applications other than chlorosilane exposure. For example, metal chlorides have been studied due to the presence of chlorine in many industrial processes [8, 21] and metal silicides have been studied due to their use in electronics [22]. It is generally considered that chloride formation is more problematic than silicide formation in industrial corrosion applications on account of their high vapor pressures. Table 1 shows the temperature that the vapor pressure of the metal chloride associated with many common alloying elements begins to exceed 10^{-4} atm (~10 Pa) [8, 21]. Depending on the application, this vapor pressure can be used as a “threshold” value,

above which a non-negligible amount of vaporization occurs. This demonstrates the need to protect against metal chloride formation, because metal chlorides have high vapor pressures (at elevated temperatures) and can reactively evaporate.

Species	$FeCl_2$	$FeCl_3$	$NiCl_2$	$CrCl_2$	$CrCl_3$	$CoCl_2$	$MnCl_2$	$MgCl_2$	$AlCl_3$
T(°C) at 10^{-4} atm	536	167	607	741	611	587	607	663	76

Table 1. Temperature that common metal-chloride vapor pressures exceed 10^{-4} atm (~10Pa) [8, 21].

Conversely, metal silicides are potentially protective by forming dense, well-adhered surface layers [22]. Therefore, for chlorosilane service, many industrial plants use alloys that resist chloride attack [17]; however, the implementation of expensive corrosion resistant alloys comes at great cost. The main alloying elements of both high and low cost structural metals are iron, nickel, and chromium. Because of this, the main focus of this discussion will be on how these materials interact with silicon and chlorine containing species.

Iron

Iron chloride formation has been studied extensively due to the presence of chlorine fuel impurities in many power plants, jet turbines, and other high temperature oxidizing environments. Iron chlorides can form from the interaction of iron with hydrogen chloride, chlorine, or many other chlorine containing species [23]. Iron chlorides ($FeCl_2$, $FeCl_3$) are known to be volatile at high temperature due to their high vapor pressure, causing them to reactively evaporate [8, 21, 24]. This type of interaction causes mass loss corrosion and is problematic for industry if it is not controlled. While

iron chlorides have not been extensively reported concurrently with iron silicides, there are some potential parallels with chloride formation in oxidizing environments [25]. Jacobson reported that in a mixed oxide and chloride environment at 550°C, iron will follow primarily oxidation behavior with the exception of a condensed metal chloride layer at the oxide/metal interface where the oxygen potential is low [24]. Additionally, there is some volatilization of various iron chloride species which must be accounted for. The exception to this trend is at low bulk oxygen partial pressure. In this case, there is enhanced oxidation, likely due to some porosity in the oxide layer caused by chloride volatilization. It is likely that this phenomenon will occur in mixed chloride/silicide forming environments due to the similar combination of a condensed metal silicide and a volatile metal chloride.

Iron silicides have also been studied and their formation generally tends to be less problematic from a corrosion standpoint. There are several ways to form iron silicides including gas-solid interactions and solid-solid interactions. In either case, the result is typically a series of stratified surface layers that develop in the iron substrate with different stoichiometry based on the gradient of silicon activity [26, 27]. A few solid-gas interactions of note came from Rebhan, et al. when they studied the chemical vapor deposition (CVD) of silicon onto iron [28, 29]. The goal of their research was to characterize the CVD process using silane as a feed gas to deposit silicon and then oxidize it to form silica (SiO_2). The silica would then act as an adhesion layer between the iron substrate and a polymer coating. They found that they formed silicides, primarily Fe_3Si, rather than depositing silicon during their experiments at less than 600°C. During

experiments at 800°C and higher, silicon was deposited on to the iron substrate, and it subsequently diffused in to the iron. They then oxidized this deposited silicon to form their silica adhesion layer. Klam, et al also published a solid-gas interaction study that looked at the influence of silicon source [30]. With a silane source the, silicon tends to go into solution in the iron prior to preferentially forming Fe_3Si at the grain boundaries. With a STC silicon source, they found primarily Fe_3Si after exposure with some amount of open porosity. This open porosity was not present in the experiments with silane, and it is suspected that they form from the reaction of either iron or iron silicide to form volatile iron chloride. This study was also focused on CVD applications, so the exposure temperatures were quite high (750-1100°C).

Baldwin and Ivey studied the solid-solid interaction of silicon and iron by annealing diffusion couples in a vacuum at 700-800°C and times up to several months [31]. Their first experiment involved a Fe-Si couple, and they found that there are 3 very distinct iron silicide compounds that form; Fe_3Si, FeSi, and $FeSi_2$ developing in that order. There is very little concentration variation within the layers, contrary to the Fe-Si phase diagram. Their next experiment involved a Fe_3Si-Fe diffusion couple [32]. In this couple, they were able to form a slow growing non-stoichiometric $Fe_{3+x}Si_{1-x}$ layer as predicted by the phase diagram. Their conclusion from this work was that stoichiometric Fe_3Si grows preferentially and more quickly than non-stoichiometric $Fe_{3+x}Si_{1-x}$. This result is valuable because it lays the framework for understanding the iron silicide formation and growth processes.

Nickel and Chromium

Chromium and nickel also form metal-silicides and metal-chlorides contingent on the environment. It has been reported that nickel in pure HCl at temperatures greater than 500°C results in a net mass loss [33, 34], and in the presence of silicon at temperatures greater than 500°C, forms various nickel silicides, which are stable and adhered well to the substrate [22, 35]. Additionally, chromium is known to form $CrCl_2$ in the presence of HCl at temperatures above 500°C [36]. However, this $CrCl_2$ scale is only somewhat protective below 600°C, and above 600°C, it readily evaporates. There are several chromium-silicon species (CrSi, CrSi2, Cr3Si, Cr5Si3) however, they require extreme temperatures (~1200°C) to form [22, 37].

Additional Prior Research

The behavior of a variety of metals and alloys in a chlorosilane environment has been investigated by Mui using a packed bed reactor to chlorinate metallurgical grade silicon [17]. Samples were exposed to an environment at 500°C and 2.07 MPa containing 70.6% STC, 28.1% TCS, 0.8% DCS, and 0.5% HCl as measured by an inline gas chromatograph. The metals tested include nickel, copper, Alloy 400, carbon steel, 304 stainless steel, Incolloy 800H, and Hastelloy B-2. Results indicated that many of the alloys tested formed a silicide layer that acted as a protectant from future HCl attack. However, the dependence of silicide formation on time, temperature, or gas composition was not reported. Corrosion rates were calculated based on linear reaction kinetics; however, the author stated that linear kinetics may not be a valid assumption. In order to be applied to industry, it is imperative that engineers understand how time, temperature,

and composition influence corrosion, so that it can be predicted and controlled. Without this knowledge, users risk creating volatile metal chlorides which may lead to excess corrosion and equipment failure, or excessively thick metal silicide surface layers that may spall and consume base metal.

Acker, et al. has also studied the formation of transition metal silicides in chlorosilane environments with their primary focus being nickel [38, 39]. They proposed several reactions in the metal-chlorosilane system that can take place to form metal silicides. The first is the direct reaction of a metal with STC to form a silicon rich metal silicide as modeled by Equation 28. The second reaction of interest is the formation of a metal-rich metal silicide from a silicon-rich metal silicide and a metal (II) chloride as modeled by Equation 29.

$$xM\,(s) + ySiCl_4\,(g) + 2yH_2\,(g) \rightarrow M_xSi_y\,(s) + 4yHCl\,(g) \quad (28)$$

$$M_xSi_y\,(s) + zMIICl_2\,(s) \rightarrow M_{x+z}Si_{y-0.5z}\,(s) + 0.5zSiCl_4\,(g) \quad (29)$$

From these equations, Acker and his colleagues were able to thermodynamically predict several layers of nickel silicide that are stable when nickel is exposed to STC and then experimentally verify their predictions. In addition to these findings, Acker also studied the behavior of transition metal silicides in anhydrous HCl, although for a different application than what is addressed here [38, 39]. Acker was interested in using HCl to form more metal-rich metal silicides as modeled by Equation 30.

$$M_xSi_y\,(s) + 3HCl\,(g) \rightarrow HSiCl_3\,(g) + M_xSi_{y-1}\,(s) + H_2\,(g) \quad (30)$$

This reaction is applicable in corrosion because it shows that there is some interaction between metal silicides and HCl. This implies that metal silicides are not fully

protective, but they may partially impede chloride attack. Additionally, it shows that chloride content can significantly alter corrosion mechanisms in chlorosilane systems. Acker's work was aimed at making metal silicides for the electronics industry, not as a corrosion product. A study more focused on the corrosion aspect of these systems is crucial for continued advancement and optimization in industries that use chlorosilanes. Although Acker established a framework for studying other metals in these environments, reported results were limited to nickel. Iron and chromium are arguably more critical structural alloying elements partly due to their lower costs and partly due to their manufacturing ease. These advantages, along with the goal of exploring corrosion behavior of low cost alloys in chlorosilane environments, further motivates this study.

EXPERIMENTAL METHODS

The methodologies for corrosion exposures, analyzing corrosion layers, and interpreting results are broken up in to three sections. The first section describes the corrosion exposure. Next, the surface analytical and sample processing equipment is described in the context of its use for corrosion layer evaluation. Finally, the construction and utility of predominance diagrams and chemical equilibrium is explained as it relates to corrosion environments and corrosion products.

Corrosion Exposure

Corrosion testing was performed in a custom tube furnace system constructed in the Montana State University High Temperature Materials Laboratory. This testing system can expose several samples to a controllable chlorosilane environment at a variety of temperatures, times, and gas compositions. The test setup is schematically illustrated in Figure 8.

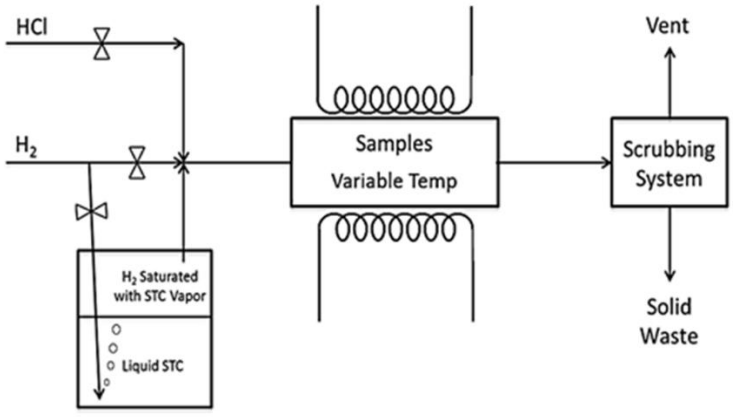

Figure 8: Schematic of the furnace system used for high-temperature chlorosilane exposures

In this test system, an adjustable amount of H_2, controlled by a calibrated Alicat Scientific mass flow controller, was delivered via needle through a rubber septum and bubbled into the bottom of a 1 liter bottle containing liquid STC. As the H_2 bubbles rose through the STC, they became saturated with STC, making the head space a consistent mixture of H_2 gas and STC vapor. This vaporized the STC and forced the saturated STC/H_2 mixture to flow out of the bottle through a separate needle in the bottle head space exiting the septum. This saturated STC/H_2 stream was combined with a variable amount of hydrogen chloride and makeup hydrogen, both controlled with individual mass flow controllers. The makeup hydrogen permits control of the STC/H_2 mole ratio, while the hydrogen chloride was used to represent typical concentrations found in industrial processes. The gas stream was flowed over the samples in the tube furnace, and then to the scrubbing system. The scrubbing system had a built-in pressure relief system that released if it exceeds approximately 10 psig (~70 kPa). The pressure of the STC/H_2 line was not explicitly measured due to the incompatibility of many laboratory scale pressure gauges with STC.

In this testing system, a quartz tube (placed within a tube furnace) with an inside diameter of 26.8 mm was used with flat metal samples placed within. This allows for gas flow on both sides of the samples so that the entire surface area was subjected to the corrosive exposures. The gas composition of the test system was controlled by adjusting the relative amounts of makeup hydrogen and hydrogen chloride to dictate the mole fraction of each component supplied to the system. While the flow rates of hydrogen and hydrogen chloride could be taken directly from the mass flow controllers, the amount of

vaporized STC was calculated based on the difference in the STC bottle mass before and after an experiment. For this calculation, the assumption was made that none of the STC leaked through the septum. This was generally a safe assumption because leaks were easily detected due to the buildup of silica anywhere STC interacted with water vapor.

The amount of STC vaporized in to the hydrogen gas stream can be estimated using Antoine's equation (Equation 31). The Antoine equation parameters for STC at room temperature are A=4.82892, B=1616.546, and C=5.305 [40]. From this information, at 298K, the vapor pressure of STC is 0.315 bar. Assuming a total pressure of 1 bar in the head space of the bottle, the hydrogen and STC mole fractions are 0.685 and 0.315 respectively. While this is an important calculation to understand, variations in room temperature and pressure make the previously described STC mass measurements necessary. However, the implication of this relationship is that the assumption of constant STC vaporization is valid. A typical total mole ratio of H_2:STC:HCl with the addition of make-up hydrogen was approximately 0.730:0.252:0.018, with the hydrogen flow rate totaling ~60 SCCM. This leads to a total flow rate of approximately 82 SCCM and an average velocity of 14.5 cm/min through the tube furnace at standard temperature and pressure.

$$log_{10}p = A - \frac{B}{C+T} \tag{31}$$

Corrosion tests were run between 0 and 200 hours; using this range of testing times, important information regarding the kinetics and thermodynamics of corrosion reactions could be assessed. Exposure temperatures varied from 500-700°C, allowing for temperature dependences to be determined. HCl mole fraction and the presence of

metallurgical grade silicon were also variables that were controlled. Both of these factors changed the corrosion environment to replicate different processes in polysilicon manufacturing. It was predicted that increased HCl will increase chloride formation and vaporization while the presence of metallurgical grade silicon will increase the silicon activity, promoting silicide formation.

Analytical Techniques

Pre- and post-exposure surface and gravimetric analyses were performed in order to detect changes in sample composition as a result of the corrosion exposure. Surface analysis included field emission scanning electron microscopy, energy dispersive x-ray spectroscopy, and x-ray diffraction. These analyses combined with gravimetric analysis and cross sectioned sample preparation provided data to explain the interaction of sample materials and chlorosilanes at high temperatures.

Field Emission Scanning Electron Microscopy

Field Emission Scanning Electron Microscopy (FEM, FE-SEM) was performed using a Zeiss Supra 55VP. A field emission electron microscope works by producing and focusing an electron beam on an area of a sample approximately 10 nanometer in diameter [41]. When the electron beam interacts with the sample, there are several emissions including secondary electrons, backscattered electrons, and characteristic x-rays. The secondary electrons are relatively low energy which only allows them to escape from approximately the first 100 nanometers of a surface. Therefore, they are very good for imaging the surface topography. Their intensity is measured by a secondary electron

detector that detects the location of the emitted electrons and their relative intensities which is then correlated to surface topography. Backscattered electrons are of relatively high energy; up to the energy of the incident electron beam. Their relative energy depends on the atomic number, making them useful for imaging contrast in atomic number (z-contrast). Backscattered electron images were not a routine part of corrosion layer analysis for this study, but it was often employed to supplement the work.

In all electron imaging, the sample surface must be sufficiently conductive and electrically grounded so that the incident electron beam does not cause charging. In metallic samples, this is not an issue because the metal samples are conductive and are mounted via conductive carbon tape to the ground. However, some corrosion scales were not conductive which caused charging. This issue was alleviated by coating the surface of the sample with a thin layer of iridium in a sputtering process. The iridium was sufficiently thin that it did not alter the topography of the surface, yet thick enough that it provided a path to ground for the incident electrons.

Energy Dispersive X-Ray Spectroscopy

Energy Dispersive X-Ray Spectroscopy (EDS, EDX) was used in conjunction with the FEM system. EDS detects the energy of emitted characteristic x-rays using silicon based detectors [41]. EDS is a very fast chemical analysis technique that can detect relative atomic concentrations in the electron beam/specimen interaction volume. It is considered a bulk characterization technique because the x-rays have enough energy to escape from a depth of 2-3 microns depending on the energy of the incident electron beam and the material of interest. It is recommended that the incident electron beam be a

minimum of 2 times the energy of the primary characteristic x-rays of interest. For this application, a beam voltage of 15 keV was generally sufficient. In this application, EDS was used without standards. This limits elemental quantification to about 1 atomic percent. Therefore, results should be primarily interpreted qualitatively. The primary use of EDS was rapid identification of atomic species and identification of areas with variable atomic concentrations. The EDS system in the Imaging and Chemical Analysis Laboratory at MSU is capable of spot scans, line scans, and area scans. Line and area scans are generally of interest because they allow the user to inspect for compositional variation. A specific application of this may be in analyzing the composition of a corrosion product. Variation or stratification in corrosion layers may provide some insight into how the corrosion layers form and grow.

X-Ray Diffraction

X-Ray Diffraction (XRD) is a technique most often used to characterize the crystalline structure of a sample [42]. The primary advantage of XRD is that it directly measures the crystalline lattice spacing of a material rather than the elemental composition. This allows XRD to differentiate between two materials that have the same atomic composition but are different phases. The basis for XRD is Bragg's law. Bragg's law predicts angles that will generate constructive interference of diffracted x-rays based on spacing between crystalline lattice planes. The equation for the Bragg condition is displayed as Equation 32 [42]. In this equation, $n\lambda$ represents integer multiples of the incident x-ray wavelength, d is the crystalline plane spacing, and θ is the angle of incidence. When the two sides of the equation are equal, there is primarily constructive

interference which causes the x-rays to be diffracted and detected. Because the incident wavelength is generally fixed, the diffraction angle depends only on the crystalline plane spacing. Therefore, a plot of x-ray counts per second versus angle can be generated with every angle that causes an increase in counts per second correlating to a crystalline plane distance. These patterns can then be compared to known patterns and the crystalline structure and size can be determined. Because crystalline structures and sizes are unique, the crystalline phase can generally be inferred.

$$n\lambda = 2dsin(\theta) \tag{32}$$

The XRD system employed in this testing was a Scintag X1 diffraction system that uses Jade software for pattern analysis. This system has a copper Kα x-ray source that generates a monochromatic x-ray with a wavelength of 1.5406 Angstroms. The interaction volume, depending on the angle of the source and detector, is approximately 1 mm by 1 mm by 10 microns deep which makes XRD primarily a bulk analysis technique.

Cross Sectioning and Polishing

Metallographic cross sectioning and polishing of corroded samples was accomplished with an Allied High Tech cross sectioning and polishing system. A polished and cross sectioned sample allows for microscopy and elemental analysis across the depth of the sample. This provides some insight into how a corrosion layer may form and grow on a metal. Cross sections were prepared by first mounting the corroded sample in epoxy with the corrosion layer next to a glass slide to protect the layer. The sample was then cut with a diamond saw and polished using progressively finer polishing paper. Silicon carbide based polishing paper was used up to 1200 grit with aluminum oxide

lapping films used subsequently. Both of these were used with water based lubricants. This adds some potential error in that water soluble corrosion products, specifically metal chlorides, could be washed away by the lubricants. Therefore, it is noted that any voids seen in the corrosion layers may be the result of metal chlorides being unintentionally removed. However, metal silicides are not water soluble and remain intact through the cross sectioning and polishing process. The final surface roughness was generally less than 0.1 microns. This smooth finish allowed for FEM and EDS analysis on the cross section, permitting compositional and morphological variation analysis as a function of depth. Cross sectioning and polishing analysis was generally the final step in sample analysis because it is a destructive technique.

Gravimetric Analysis

Gravimetric analysis is essential when studying corrosion behavior of metals because it is the first indicator of how the metal behaved in the environment. Mass gains generally indicate the formation of a stable corrosion layer, mass losses generally indicate the formation of a volatile corrosion product, and zero mass change could indicate that either the material did not corrode or there was some combination of mass gain and mass loss phenomena that canceled each other out. In this study, ex-situ gravimetric analysis was performed using a Sartorius microbalance with 2 microgram precision. The mass of the samples was taken before and after exposure with the change in mass indicating whether primarily stable or volatile corrosion products were formed. The change in mass of the samples was divided by the surface area of the samples to get a geometrically independent mass change. Surface area was calculated by measuring the dimensions of

the samples using calipers with 0.01 mm precision and performing the appropriate surface area calculation based on the sample shape.

Once the area-specific mass change had been calculated, two data transformations were done in order to compare mass change data with theoretically predicted results. The first transformation was for experiments aimed at detecting the temperature dependence of corrosion. For these experiments, the natural log of mass change after a constant time interval was plotted against 1000/(absolute temperature) to check for changes in corrosion mechanism. If the samples experienced the same corrosion mechanism at all temperatures, the result of this plot will be a straight line with the slope of the line being indicative of the activation energy of that mechanism. Deviations from this line indicate a change in activation energy likely caused by a change in corrosion mechanism. The other data transformation applicable to these experiments was for time dependent data to check for fit with parabolic kinetics. For this data, the specific mass change was plotted against the square root of exposure time at a constant temperature. If the data are purely parabolic, this plot will result in a straight line that goes through zero with the slope of that line equal to the square root of the parabolic rate constant. Deviations from this line represent non parabolic kinetics.

Error bars in all figures displaying gravimetric results represent a 95% confidence interval as calculated from samples run in triplicate. One primary source of gravimetric error was material loss between the exposure and mass measurement. Very thick surface silicide layers occasionally spalled off of the samples during handling steps while surface chloride layers sometimes smeared off. These fragments of broken or smeared layers

were included in the mass measurements, however, this was inevitably a potential source of error and the main reason why error bars got larger at higher temperatures, longer exposures, and higher mole fractions of HCl.

Thermodynamic Calculations

Thermodynamic calculations were a critical portion of this work in that they were able to help explain equilibrium corrosion behavior. The majority of the calculations were done using FactSage software, a thermodynamic calculation package that is commonly used for condensed and gas phase simulations. There were two main types of information from FactSage that were useful for this work; predominance diagrams and chemical equilibrium. They are based on the same types of calculations, but the output is in a different format. The basics of the calculations will be discussed here, but it is noted that all thermochemical calculations for this work were done using the computer program. Therefore, only the calculation structure is discussed along with the limitations of using this type of tool.

For the generalized chemical reaction described by Equation 33, the Gibbs free energy change of the system, $\Delta G'$, can be written as Equation 34 where ΔG° is the free energy change when all species are present in their standard states and a is the thermodynamic activity. The standard free energy change is expressed for the reaction by Equation 35. The standard molar free energies of formation necessary to calculate the free energy change in Equation 35 can be found in tabulated form for many compounds.

At equilibrium, $\Delta G'$is equal to zero, reducing Equation 34 to Equation 36. The equilibrium constant of the system, K_{eq}, is defined as Equation 37.

$$aA + bB \rightarrow cC + dD \tag{33}$$

$$\Delta G' = \Delta G^0 + RTln(a_C^c a_D^d / a_A^a a_B^b) \tag{34}$$

$$\Delta G^0 = c\Delta G_C^0 + d\Delta G_D^0 - a\Delta G_A^0 - b\Delta G_B^0 \tag{35}$$

$$\Delta G^0 = -RTln(a_C^c a_D^d / a_A^a a_B^b) \tag{36}$$

$$K_{eq} = a_C^c a_D^d / a_A^a a_B^b \tag{37}$$

These equations are now used to construct a single line on a predominance diagram as an example of the solution technique. This line represents the silicon activity where both Fe and Fe_3Si exist. In other words, this line traces the activity of silicon where both Fe and Fe_3Si have an activity of 1. The reaction is modeled by Equation 38 which shows the formation of Fe_3Si from pure iron and silicon. The equilibrium constant, $K_{eq}^{Fe_3Si}$, can then be defined and simplified due to the activity assumptions as shown in Equation 39. $K_{eq}^{Fe_3Si}$ can then be written in terms of the free energy of formation of Fe_3Si (Equation 40) which is tabulated in the FactSage database. Solving for the activity of silicon reveals the solution in known quantities (Equation 41). This solution is in logarithmic terms so the plotting can display large ranges of data. This solution technique can then be applied to other species in the iron-silicon-chlorine system including FeSi, $FeSi_2$, and $FeCl_2$. A resulting predominance diagram is shown as Figure 11, and will be discussed later in terms of corrosion exposure results.

$$3Fe + Si \rightarrow Fe_3Si \tag{38}$$

$$K_{eq}^{Fe_3Si} = a(Fe_3Si)/a(Si)a(Fe)^3 = 1/a(Si) \tag{39}$$

$$\log\left(K_{eq}^{Fe_3Si}\right) = -\Delta G^0/2.303RT \quad (40)$$

$$\log\left(K_{eq}^{Fe_3Si}\right) = -\log(a(Si)) \quad (41)$$

Calculations for gas phase chemical equilibrium can also be easily assessed using FactSage. Chemical equilibrium is necessary to calculate because as a mixture is heated from room temperature to exposure temperature, the mixture composition very likely changes. In the case of chlorosilane corrosion, an input stream of just hydrogen and silicon tetrachloride may change to include many other chlorosilane species when heated, which may change the silicon or chlorine activities, which will in turn change the corrosion behavior. Also, chemical equilibria with the addition of a condensed phase can be calculated. This may be used to model the situation in a reactor where condensed phase silicon is added to the vapor stream to change the composition.

The process for calculating gas phase chemical equilibrium utilizes the same formulas as those required for the predominance diagram construction. While chemical equilibrium can be calculated by hand for simple systems, complex systems require an iterative computational routine that minimizes the Gibbs Free Energy of the system based on Equations 34, 35, and 36. This routine has been established by the FactSage developers for a variety of systems, to simulate equilibrium compositions and properties.

While computational thermodynamics is a useful tool, it does have some limitations. The first consideration is that it is assumed that chemical equilibrium is reached. In a high temperature (>500°C) gas environment, this is often the case. However, the interaction of the gas environment with solids, as is the case in a corrosion situation, means that equilibrium takes longer to be established. Furthermore, it is

assumed that the input stream is known exactly. That is likely not the case, as there are impurities present in the hydrogen, STC, HCl, and the rest of the system in general. These impurities can have a significant effect on the equilibrium composition of the gas stream, which can significantly alter the corrosion behavior. Finally, the computation of chemical equilibrium heavily relies on tabulated input data. Often this data is sufficiently accurate due to the widespread use of these chemicals. However, it is likely that there is some error associated with the calculation of tabulated thermochemical data which will be transferred to the calculation of chemical equilibrium. Due to these and other concerns, the thermochemical calculations for this work will largely be used to help explain experimental results and observations rather than for quantification.

CHLOROSILANE CORROSION OF AISI 316L

In the chlorosilane industry, high nickel alloys are generally used to handle chlorosilanes at high temperatures. These nickel alloys are used because they are known to resist chloride attack. However, they also contribute greatly to the cost of chlorosilane products. In this study, AISI 316L was exposed to a variety of chlorosilane environments to test the feasibility of using a low cost iron based alloy in chlorosilane service. This information has been published in the *Journal of the Electrochemical Society* [43] and the *Electrochemical Society Transactions* [44, 45].

AISI 316L Introduction

AISI 316L is an austenitic stainless steel with a nominal composition of 0.03 max wt% C, 2 max wt% Mn, 0.045 max wt% P, 0.030 max wt% S, 1 max wt% Si, 16-18 wt% Cr, and 10-14 wt% Ni, with the balance Fe. Samples for this testing had a mirror finish prior to cutting and handling steps. They were cut to approximately 12 mm x 12 mm x 1 mm squares, deburred, and cleaned with isopropyl alcohol to remove any cutting fluids. Samples were generally run in triplicate.

Corrosion tests were run between 0 and 200 hours; using this range of testing times, important information regarding the kinetics and thermodynamics of corrosion reactions can be assessed. Exposure temperatures varied from 500-700°C, allowing for temperature dependences to be determined. Finally, the total HCl mole fraction was varied from 0-0.6 while holding the STC and hydrogen mole fractions relatively constant. HCl mole fraction is considered an important variable for several reasons. It is suspected

that as the HCl mole fraction increases, the amount of metal silicide formation decreases, and correspondingly, the formation of metal chlorides increases. Because metal silicides may be considered a passivation layer and metal chlorides a volatile product, it is extremely important to understand the amount of HCl that can be present while still forming metal silicides.

AISI 316L Corrosion Exposure Results

The results of the AISI 316L series of exposures will be presented in three sections. These sections separately investigate the dependence of AISI 316L chlorosilane corrosion on the composition of the chlorosilane stream, the temperature of the exposure, and the time of exposure.

Composition Dependent Results

The first part of this study was looking at the dependence of corrosion on input mole fraction HCl. Mole fraction HCl was considered the control variable because it directly changes the chlorine activity in the system and it is easy to control via mass flow controller. For these tests, the H_2:STC mole fractions were held approximately constant at 0.73:0.25 while the HCl mole fraction was varied to specified values. The time of exposure was held constant at 100 hours and two series of exposures, one at 550°C and one at 600°C, were performed. The gravimetric results from this testing are shown in Figure 9. This discussion will first focus on the 550°C results and then move to the 600°C results.

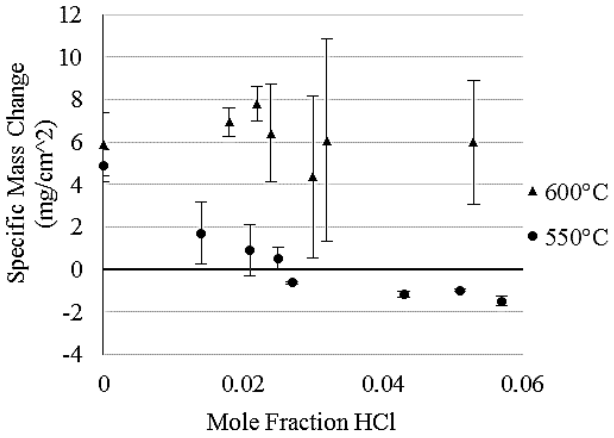

Figure 9: Gravimetric analysis from variable HCl testing at 550 and 600°C. The error bars represent a 95% confidence interval.

From this graph, it is clear that at 550°C, specific mass change decreases with increasing amounts of HCl. This phenomenon can be explained by suggesting that without HCl in the system, iron silicide formation is the dominant reaction. Iron silicide is stable and well adhered to the sample surface, causing a net mass gain. This reaction is modeled by Equation 42. When a larger amount of HCl is added to the system, iron and chromium chloride formation become the dominant reactions. One type of iron chloride formation in this system is modeled by Equation 43. The chloride resulting from this reaction is volatile at 550°C as shown in Table 1. In reality, it is likely that both of these reactions plus many more silicide/chloride forming reactions happen concurrently with the HCl content dictating which are dominant. This helps explains the intermediate values of mass gain with small amounts of HCl.

$$Fe + SiCl_4 + 2H_2 \rightarrow FeSi + 4HCl \quad (42)$$

$$Fe + 2HCl \rightarrow FeCl_2 + H_2 \quad (43)$$

The presence of chlorine and silicon containing species was verified by FEM and EDS. Figure 10 shows FEM micrographs and EDS spot scan locations for exposures at several different concentrations of HCl. EDS results for all FEM micrographs are shown in Table 2. As was predicted by the gravimetric analysis, primarily metals and silicon were detected after exposure at low concentrations of HCl indicating metal silicide formation. As HCl concentrations increase, there is more residual chromium and chlorine on the sample surfaces. This trend continues until very high HCl concentrations at which point there are negligible amounts of detectable silicon species present. It is important to note the large differences in surface morphology between the silicon containing and chlorine containing species. Microscopically, the iron and silicon rich areas appears to have a highly crystalline structure while the chromium and chlorine rich areas are amorphous and friable. This is consistent with macroscopic observations as well. When handling the primarily chloride forming samples, it was clear that the surface chloride layers were wax-like and could be wiped away. The silicide layers were much harder and could only be removed with a considerable amount of force. In surface analysis, the presence of chromium chloride was used as an indicator of overall chloride formation due to low vapor pressure at the exposure temperatures (Table 1). In addition to using chromium chloride as an indicator of chloride formation, the condensate at the cool end of the tube furnace was collected and analyzed with FEM/EDS. Semi-quantitative EDS analysis revealed an atomic composition consistent with stoichiometric $FeCl_2$.

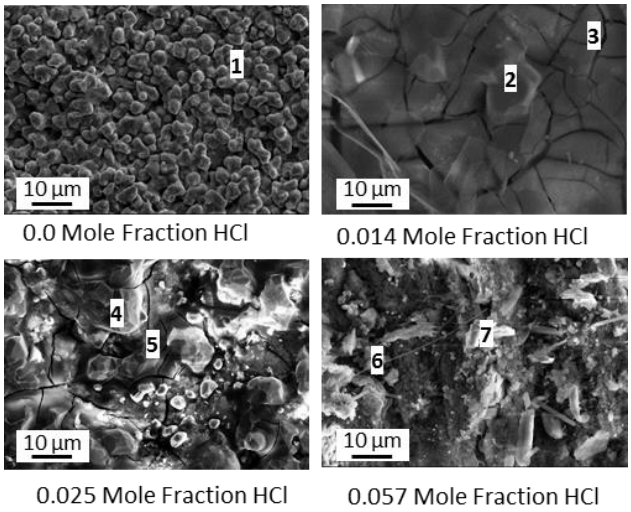

Figure 10: FEM micrographs and EDS spot scan locations for several AISI 316L samples after exposure to chlorosilane environments with various amounts of HCl at 550°C after 100 hours of exposure. EDS data is displayed in Table 2 which shows spots 1, 2, and 4 containing primarily Fe and Si and spots 3, 5, 6, and 7 containing significant amounts of Cr and Cl.

	Atomic %					
Spot	**Fe**	**Cr**	**Ni**	**Si**	**Cl**	**O**
1	32	1	3	34	0	29
2	74	2	6	18	0	0
3	14	9	0	5	8	65
4	70	2	9	19	1	0
5	1	17	0	0	18	63
6	0	9	2	14	16	58
7	1	33	0	1	45	20
8	30	25	3	12	0	30
9	62	16	6	2	0	15
10	52	16	6	2	0	24
11	59	10	2	15	4	11
12	43	5	8	44	0	0
13	48	7	1	42	0	0
14	8	2	1	90	0	0
15	73	13	12	5	0	0
16	44	7	2	47	0	0
17	46	6	2	42	0	3

Table 2: EDS results for spots labeled in FEM micrographs in Figures 10, 13, and 15.

While the transition from forming silicides to forming chlorides was clear at 550°C, the same shift was not seen at 600°C. This observation was initially counterintuitive, as it was expected that the higher temperature would cause a higher metal chloride vapor pressure, leading to increased reactive evaporation. However, the predominance diagrams were able to help explain this observation. Figure 11b presents predominance diagrams for Fe in a Si-HCl-H_2 system 600°C which can be compared to the predominance diagram at 550°C in Figure 11a. These diagrams show that at low chlorine activity, silicide formation is dominant. Within the silicide dominated region, it is also clear that there are several different types of silicides, with iron-rich silicides at low silicon activity and silicon-rich silicides at high silicon activities. As chlorine activity increases, metal chloride formation is dominant. This correlates with experimental results, but what can help explain the results at 600°C comes from comparing the two predominance diagrams.

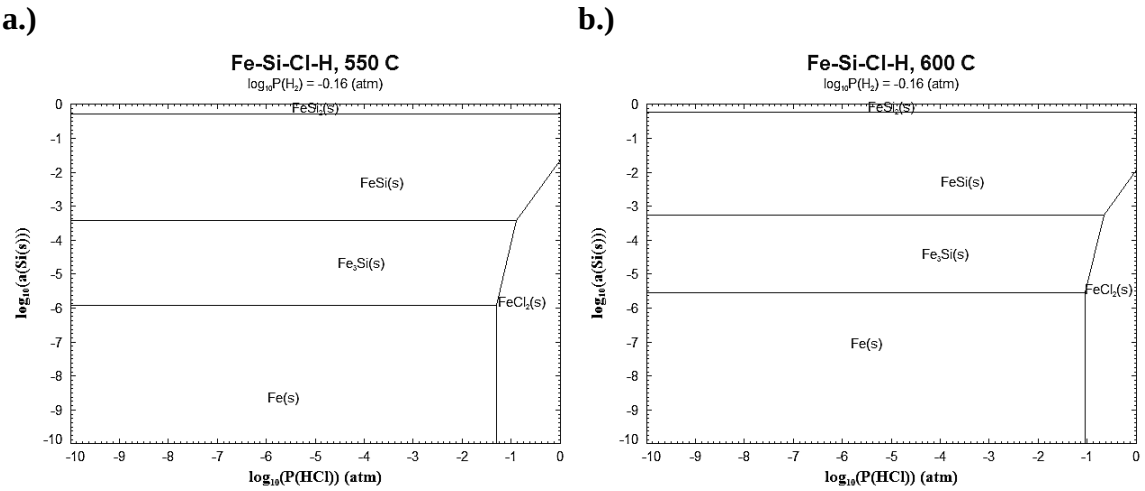

Figure 11: Predominance diagram of the Fe-Si-Cl-H system at a.) 550°C and b.) 600°C as generated by FactSage software.

It is clear that a higher temperature favors metal silicide formation as is indicated by the higher chlorine activity required to form metal chlorides. This implies that in the range of 0.03 input mole fraction of HCl corresponds to an approximate HCl activity of $\sim 10^{-1.1}$. In this range, iron is transitioning from iron silicide formation to iron chloride formation at 550°C and is consistently forming iron silicides at 600°C. This helps to explain why at 600°C, the mass change appears to be independent of HCl concentration. Based on these results, future work might include much higher HCl mole fractions to attempt to form metal chlorides at higher temperatures.

Temperature Dependent Results

The next step in characterizing AISI 316L corrosion in chlorosilane environments was to study the effect of temperature on corrosion mechanisms. For these tests, AISI 316L was exposed for 100 hours at a variety of temperatures (500-700°C) to a H_2:STC:HCl mixture with total input mole fractions equaling 0.73:0.252:0.018 respectively. Figure 12a shows the raw gravimetric data and Figure 12b shows the natural logarithm of mass change per surface area plotted against 1000/T. In general, a straight line on a plot with these axes represents a consistent corrosion mechanism with the slope of the line being representative of the activation energy for that mechanism. Because the data from this series of experiments does not form a single straight line in Figure 12b, it signifies that the rate limiting step in the corrosion process changes with temperature.

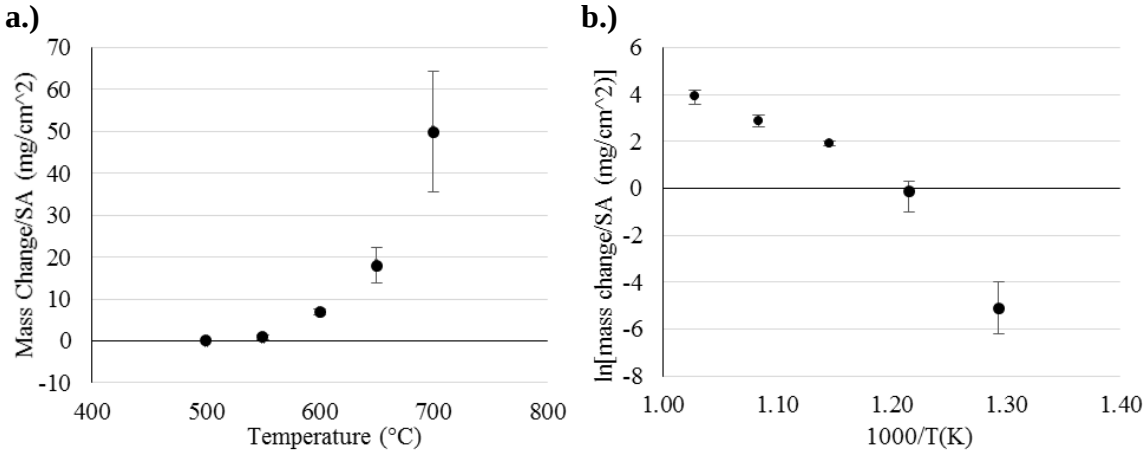

Figure 12: a.) Area specific gravimetric analysis of 316L after 100 hours at a variety of temperatures in a H_2:STC:HCl environment and b.) transformed gravimetric data used to indicate changes in corrosion mechanism. The error bars represent a 95% confidence interval.

The FEM micrographs displayed in Figure 13 also show a different surface topography for different temperature exposures. For exposure temperatures of 500 and 550°C, there are areas where EDS detected pockets of Fe and Si that are surrounded by areas consistent in composition with bare 316L. The surface topography is also significantly different for the two regions with the Fe-Si regions being highly faceted and the 316L regions appearing more polished. For the exposure temperatures at 600°C and greater, only the Fe-Si topography and composition was detected.

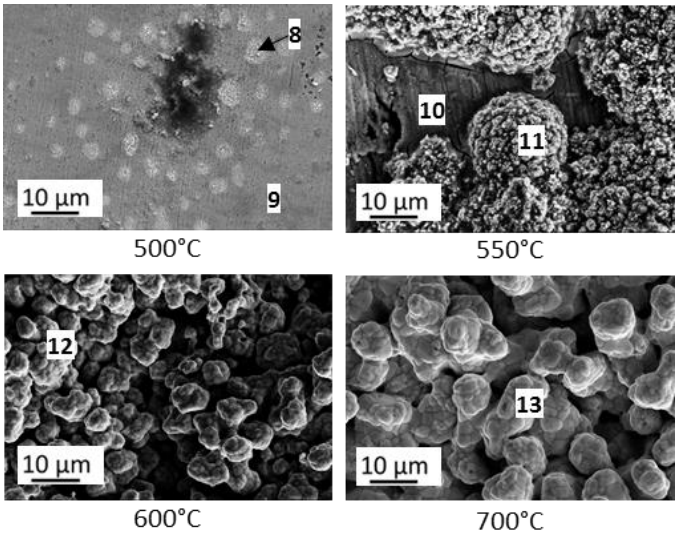

Figure 13: FEM micrographs of AISI 316L after chlorosilane exposure at a variety of temperatures. EDS results displayed in Table 2 show spots 9 and 10 consistent in composition with 316L and spots 8, 11, 12, and 13 primarily containing Fe and Si.

Based on the gravimetric data and FEM micrographs, one could argue that the lower-temperature exposures resulted in reaction-limited silicide growth while the higher-temperature exposures resulted in diffusion-limited silicide growth. This is primarily evidenced by the discontinuous silicide layer at low temperatures and a continuous silicide layer at higher temperatures. With a discontinuous silicide layer, there is bare metal readily available to react and form silicide, likely making the process reaction-limited. With a continuous silicide layer, the reacting species must diffuse through the silicide prior to reacting, likely making the process diffusion-limited. It is important to recall that these tests were performed for 100 hours. It is likely that for longer exposure times, corrosion layers formed at lower temperatures (≤550°C) will become continuous and not contain the exposed pockets of bare 316L. Conversely, short exposure times at higher temperatures (≥600°C) would likely result in discontinuous Fe-Si pockets. It is arguable that two lines could be drawn through Figure 12b, one including

the lower temperature exposures and another including the higher temperature exposures. The slope of these lines could then be interpreted as the activation energy for reaction and diffusion controlled mechanisms, respectively. However, this analysis was not done for this study due to the complex reaction mechanisms involving a highly alloyed metal and complex corrosion atmosphere. Therefore, the primary conclusions from this temperature dependent study are that the corrosion rate of AISI 316L in chlorosilane environments is highly temperature dependent, and after 100 hours, the mechanism of corrosion appears to change if the exposure is at, above, or below approximately 600°C.

Time Dependent Results

The next step in characterizing AISI 316L corrosion in chlorosilane environments was to determine the effect of time on corrosion. The time dependence of corrosion is extremely important to understand for industrial chlorosilane users because it can help predict service lifetimes and maintenance schedules. Similarly to temperature dependence, time dependent studies can help shed some light on transport mechanisms in the corrosion layer. For this series of experiments, AISI 316L was exposed for 7, 20, 98, and 188 hours at 700°C and with H_2:STC:HCl mole fraction of 0.73:0.252:0.018. These conditions were chosen because they were shown in the temperature dependent study to promote silicide formation rather than chloride formation, which is more industrially relevant to study. The raw mass change data is shown in Figure 14a.

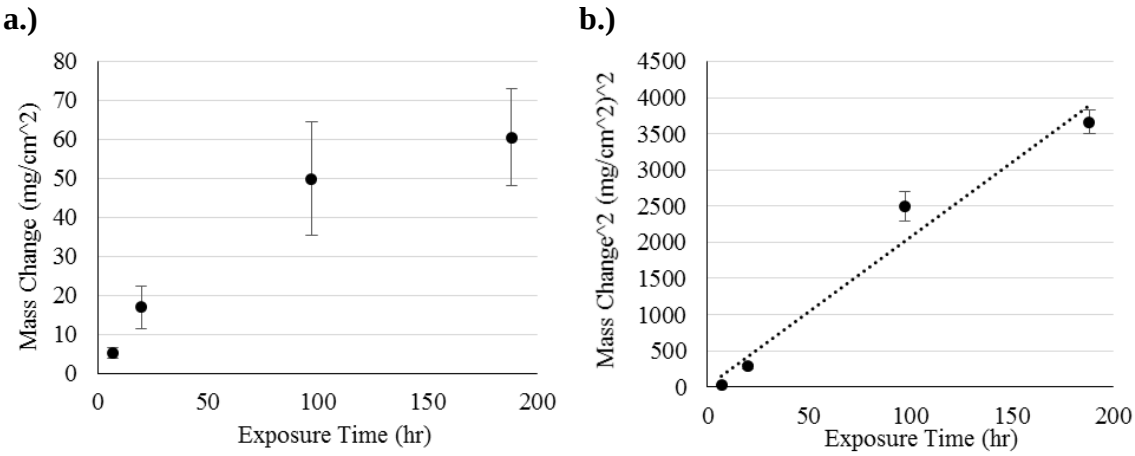

Figure 14: a.) Area specific gravimetric analysis and b.) transformed data for time dependent study of chlorosilane corrosion at 700°C. The error bars represent a 95% confidence interval.

The nearly linear relationship in Figure 14b suggests that corrosion in these conditions is diffusion controlled. However, as with the temperature dependent study, these results should be interpreted qualitatively rather than quantitatively. This is for a few reasons. First, quantitative analysis would require runs at 75 and 150 hours to add more statistical significance to the parabolic fit. Second, the substitution of corrosion layer thickness for mass change is only a numerically appropriate substitution when the corrosion layer is uniform and non-volatile. Because there are several known forms of silicide species and many chloride species are volatile, neither of these conditions are met.

As with other experiments, FEM analysis was performed on these samples to characterize the corrosion layer. The results are shown in Figure 15. This analysis confirmed that there is primarily formation of iron silicon compounds at these conditions. It is significant that at all times, there is a continuous corrosion layer on the surface. This suggests that the corrosion enters diffusion controlled parabolic growth very quickly in

these conditions. This result is consistent with Baldwin and Ivey's observations of iron silicide growth in a solid-solid diffusion couple [31].

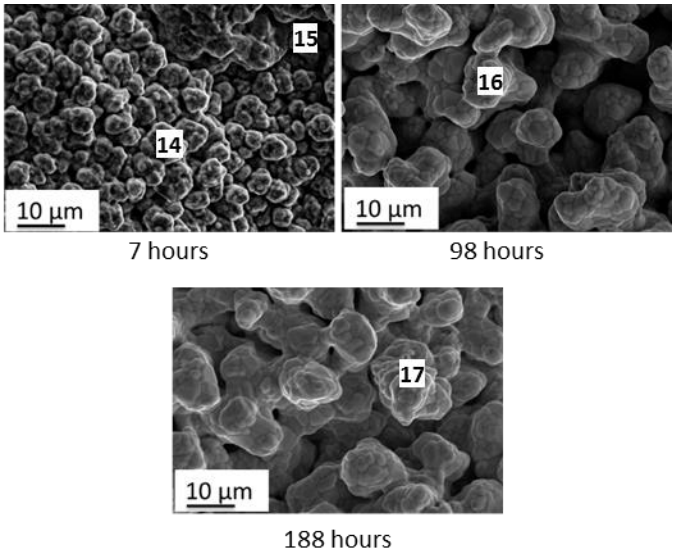

Figure 15: FEM analysis of AISI 316L samples after chlorosilane exposure at 700°C. EDS results in Table 2 showed all spots containing primarily Fe and Si. Spot 15 also contained significant amounts of Cr and Ni consistent with 316L, indicating a thinner corrosion layer at that point.

In addition to surface analysis, cross sectional analysis was performed on a sample exposed to a STC-H2-HCl environment at 700°C for 100 hours. The FEM micrograph and corresponding EDS line scans are shown in Figure 16. Figure 16 also includes a more macroscopic view of the same cross section. The macroscopic view shows delamination between the bulk metal and the corrosion layer. It is likely that this delamination occurred during the cooling process, primarily because there were no iron silicide species detected at the bulk metal interface. If delamination occurred during exposure, it is very likely that the delaminated layer would contain some pores and cracks allowing the gas stream to pass through. This would cause some metal silicide formation

on the bulk metal surface. Also, if the corrosion layer became delaminated during the exposure, it would have cutoff iron transport to the iron silicide growth interface. This would have significantly slowed the corrosion process. Because parabolic kinetics are still present at 100 hours, it is likely that iron could still transport through the iron silicide, meaning that the corrosion layer was most likely not delaminated during the exposure.

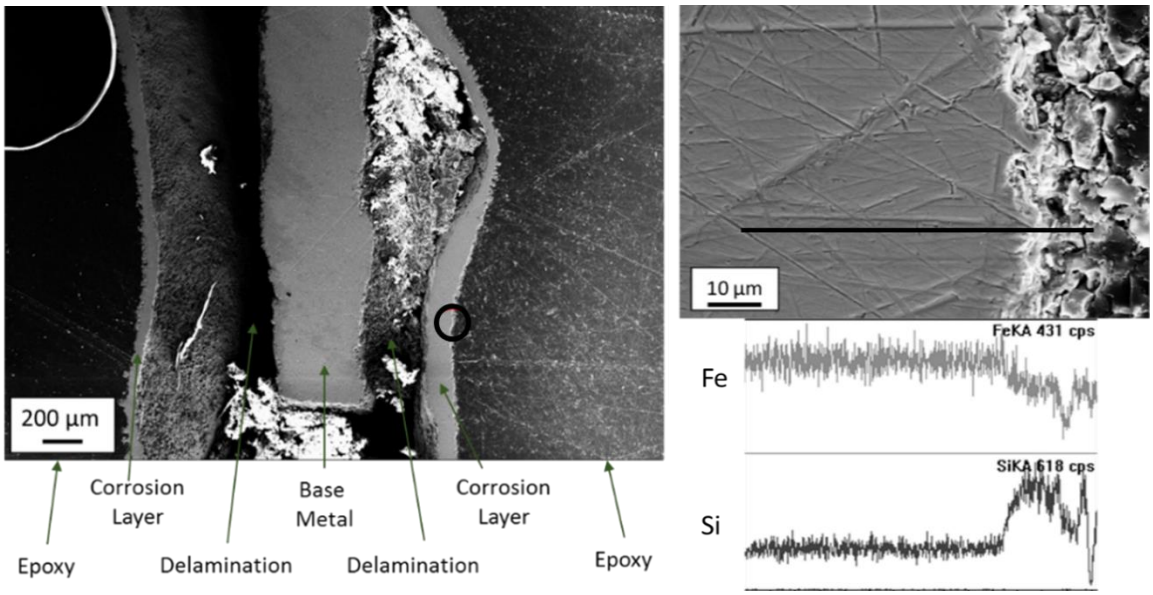

Figure 16: FEM micrographs of cross sectioned 316L sample after chlorosilane exposure. The circle on the lower magnification image indicates the location of the higher magnification image.

The higher magnification image shows the outer interface of the delaminated corrosion layer. An EDS line scan was done along the solid line, and the iron and silicon components are shown below. This line scan shows that there is a silicon rich region at the gas-solid interface, and a much thicker iron rich region through the remainder of the corrosion layer. EDS spot scans in these areas suggest that the silicon-rich region is likely FeSi and the iron-rich region is likely Fe_3Si. These phases were both predicted by the

predominance diagrams, and the EDS results indicate consistent stoichiometry. $FeSi_2$ was also predicted by the predominance diagrams, but only at very high silicon activity. Because it is not present, either these chlorosilane conditions did not produce a high enough silicon activity to form it, or it decomposed in the time that the cross section was prepared and transferred to the FEM.

AISI 316L Corrosion Exposure Conclusions

In this study, AISI 316L was exposed to a variety of chlorosilane environments as a means to study its corrosion behavior. This study found that AISI 316L can form predominately metal silicides or metal chlorides based on the amount of HCl present in the environment. It was found that higher temperatures favored metal silicide formation, as predicted by thermodynamically generated predominance diagrams. The metal silicides appeared to adhere better to the surface of the 316L when compared to the volatile metal chlorides, so their formation should be preferred in industrial processes. It was found that iron silicide formation in chlorosilane environments is likely diffusion controlled at high temperatures and long times as evidenced by the uniform, continuous corrosion layer and the parabolic growth kinetics. The temperature dependent study found an apparent diffusion-limited iron silicide formation at higher temperatures, which is consistent with other reported studies. At lower temperatures, the data indicated reaction-limited growth of the iron silicide species. Future work in this field could include the study of pure metals in chlorosilane environments in order to more fundamentally understand silicide and chloride formation of different alloying elements.

CHLOROSILANE CORROSION OF IRON

Previous work on the chlorosilane corrosion of AISI 316L looked at the implications of using an iron based alloy in high temperature chlorosilane service. This study found the there are many factors that influence the corrosion behavior of an iron based alloy in a chlorosilane environment including time, temperature, and gas composition. However, the complexities associated with studying a highly alloyed metal in a complex environment did not allow for a mechanistic investigation of the corrosion behavior. Therefore, pure iron was chosen as the subject of a fundamental chlorosilane corrosion study due to its being the primary constituent in low cost alloys. This work was published in the *Journal of the Electrochemical Society* [46].

Iron Introduction

The iron samples used in these tests were 99.6% pure with impurities of 0.025 weight % carbon, 0.03 weight % chromium, 0.04 weight % copper, 0.18 weight % manganese, 0.05 weight % nickel, 0.012 weight % phosphorous, 0.025 weight % sulfur, and 0.05 weight % silicon. They had a 1200 grit finish, were cut to approximately 12 mm x 12 mm x 1.5 mm, deburred, and rinsed with isopropanol and water prior to exposure. All exposures were done in triplicate for statistical relevance. Figures include a 95% confidence interval on the mean of the triplicate samples.

Corrosion tests were run between 0 and 100 hours; using this range of testing times, important information regarding the kinetics and thermodynamics of corrosion

reactions can be assessed. Exposure temperatures varied from 550-700°C, allowing for temperature dependences to be determined.

Iron Corrosion Exposure Results

The results of the iron series of exposures will be presented in two sections discussing the temperature and time dependence of chlorosilane corrosion. A separate section will discuss potential corrosion mechanisms at relevant temperatures and times.

Temperature Dependent Results

The first series of exposures was designed to explore the temperature dependence of iron behavior in chlorosilane environments. For these tests, iron was exposed to an input mole fraction of 0.74 H_2 and 0.26 STC for 100 hours at 550-700°C. The specific mass change from this series of exposures is displayed in Figure 17a, and the FEM micrographs are displayed in Figure 18. It appears from these figures that the three high temperature exposures resulted in very similar topography, with the higher temperature only making the nodules larger. Additionally, the corrosion scales formed at high temperature all had consistent surface compositions in line with stoichiometric FeSi as measured by EDS.

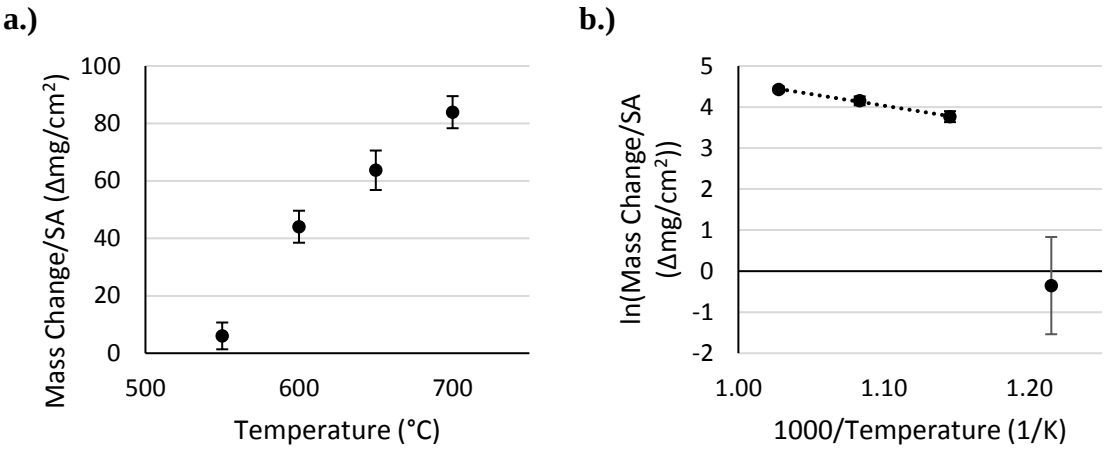

Figure 17: The a) specific mass change data and b) transformed gravimetric data for the temperature dependent study. The transformed data plots the natural log of mass change vs the inverse of absolute temperature. This transformation helps identify changes in corrosion mechanism. A linear trend line for the three higher temperature data points is displayed in b. The error bars represent a 95% confidence interval on the mean.

The exposure at 550°C resulted in a much different topography which included much finer nodules and large, high aspect ratio flakes. Additionally, the EDS spectra revealed surface regions consistent in composition with Fe and Fe_3Si. The transformed gravimetric data shown in Figure 17b shows some differences in the 550°C exposure compared to the higher temperature exposures. The three high temperature data points form a straight line when plotted versus 1/T, while the 550°C data does not fall on this line. The differences between the 550°C data and the 600-700°C data may indicate that they are experiencing different corrosion mechanisms or that they are at different stages in the corrosion process.

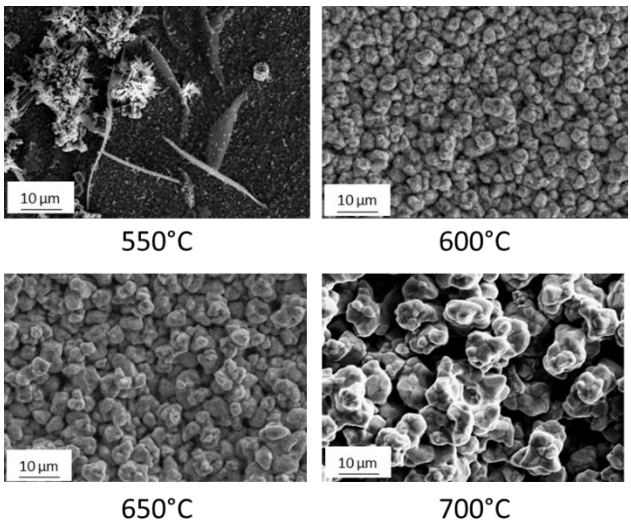

Figure 18: The plan view FEM micrographs for the temperature dependent study. These samples were exposed to a STC/H_2 environment for 100 hours at 550, 600, 650, and 700°C.

This is further supported by the XRD data displayed in Figure 19. In this figure, the XRD patterns from 40-50 two theta are displayed. This range focuses on major Fe, FeSi, and Fe_3Si peaks [47-49]. For the 700, 650, and 600°C exposures, there was a significant amount of FeSi and Fe_3Si detected. The higher temperatures made the FeSi peak more pronounced, perhaps indicating that the higher temperature formed a thicker FeSi layer on top of a Fe_3Si layer.

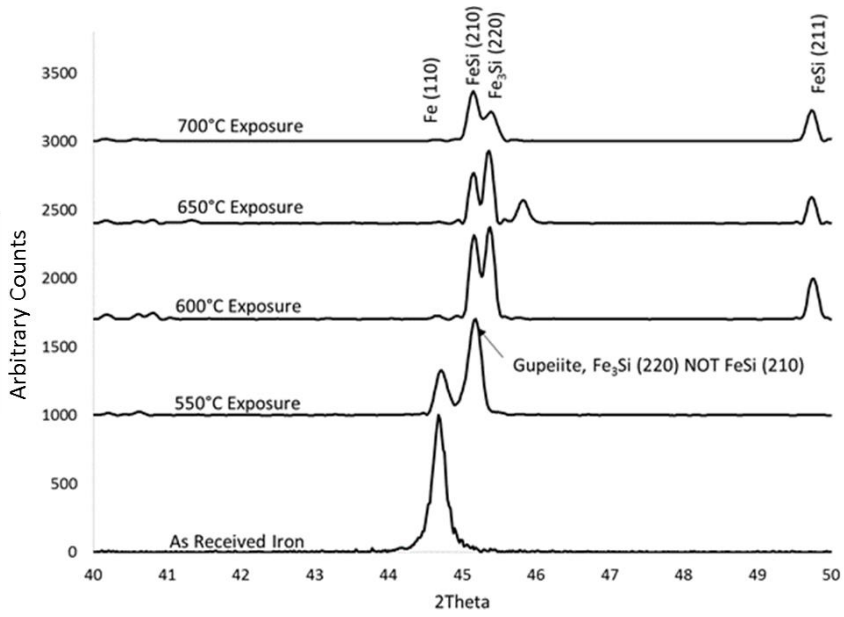

Figure 19: The XRD patterns for iron samples after exposure to chlorosilane environments at 550, 600, 650, and 700°C for 100 hours.

There is also a very small Fe peak present in some of these patterns, indicating that there is some unreacted Fe remaining in the analyzed area after exposure. In the sample after 650°C exposure, there is an unidentified peak at approximately 45.8 two theta. However, this peak and its associated species appeared to be an anomaly as it was not seen in other exposures. For the sample exposed to chlorosilanes at 550°C, there are some drastic differences compared to the higher temperature runs. The 550°C samples had a much larger Fe peak, indicating a thinner corrosion layer. The iron peak was located at a higher 2 theta value than as received iron, likely due to lattice contraction from the substitutional solution of silicon. This phenomena has been previously reported in the literature for ferritic iron-silicon alloys [50-53]. The amount of contraction due to the addition of silicon varies between studies, but the literature is in agreement with the overall trend. The measured lattice contraction of 0.003 Angstroms is in the range of

expected values for a saturated solution of silicon. Also in the 550°C study, there was a Fe_3Si (Gupeiite) [54] structure that formed rather than the Fe_3Si found at the higher temperatures. The Gupeiite peak was differentiated from the FeSi (210) peak using the presence of the FeSi (211) peak. The corroboration of the transformed gravimetric data and the XRD patterns indicate that the corrosion of iron in chlorosilanes at 550°C is mechanistically different than corrosion in a similar environment at 600-700°C.

Cross sectional images and EDS line scans were also performed in this study. Figure 20 shows the cross section of a sample after 100 hours of chlorosilane exposure at 550°C. The EDS line scan shows that there is higher silicon content on the surface that tapers to zero in the bulk iron. The total depth of silicon penetration is approximately 6 μm. This agrees with the XRD pattern that indicates both silicon in solution with iron and Fe_3Si in the sample.

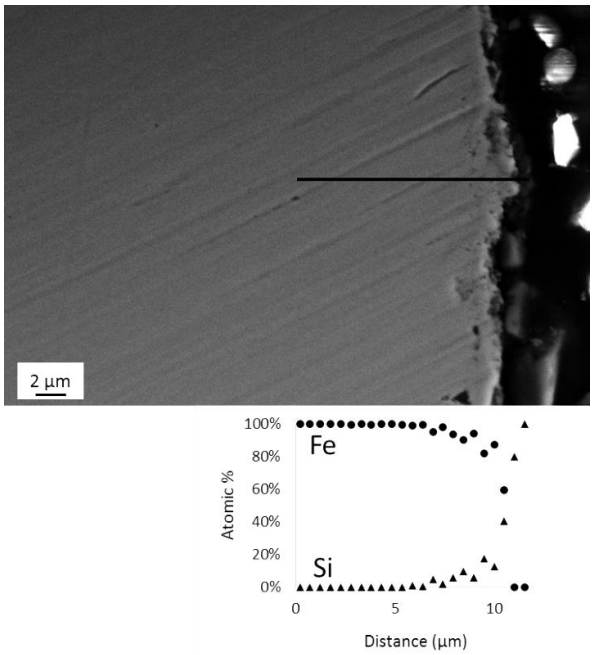

Figure 20: High magnification cross sectional image of a sample after exposure to a chlorosilane environment for 100 hours at 550°C.

The full width cross sections and line scans of samples after 100 hours at 600°C and 650°C exposures are shown in Figures 21 and 22 respectively. Because there was gas flow on both sides of the samples, it would be expected that these cross sections and EDS line scans be perfectly symmetrical. When looking at Figures 21 and 22, it appears that the images are symmetrical, but there is some asymmetry in the composition data. This could be due to errors in quantifying EDS, the detection of local non-uniformity, or some slight differences between the tops and bottoms of the sample.

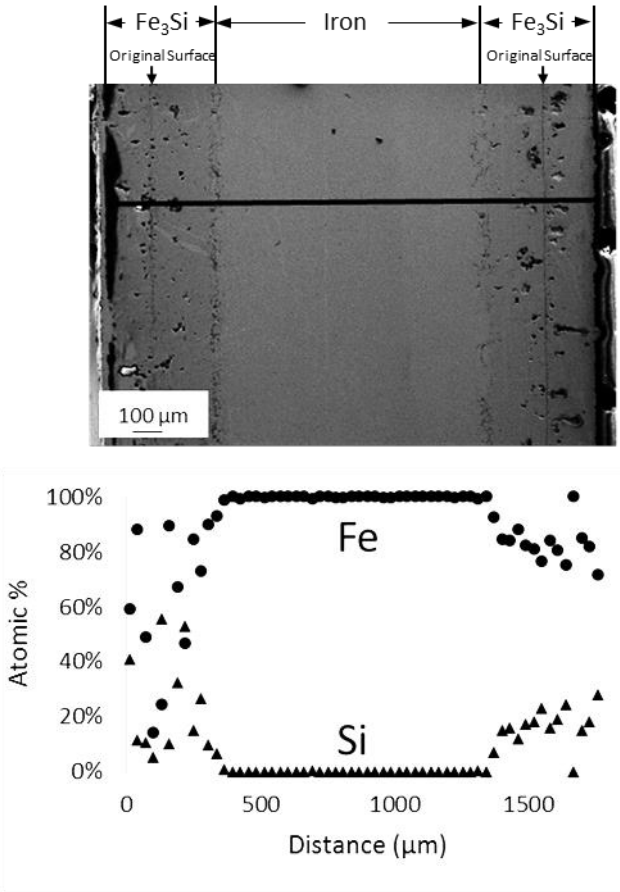

Figure 21: Full width cross sectional image of a sample after exposure to a chlorosilane environment for 100 hours at 600°C.

After 600°C exposure (Figure 21), one can see a corrosion layer that has formed on the iron substrate. Looking primarily at the right side of the cross section, it is clear that there is high silicon content at the surface that tapers down to zero in the bulk iron. Based on the atomic concentrations coupled with the XRD patterns, it is clear that the majority of the corrosion scale is Fe_3Si. The tapered Si region may represent where silicon has diffused into the iron lattice but is not present in high enough concentrations to form Fe_3Si. This trend is also present after exposure at 650°C as displayed in Figure 22. This cross section is interesting because it shows just a small internal region of pure iron remaining. The majority of the sample has been converted to Fe_3Si or iron with silicon in solution. A cross section and line scan taken after exposure for 100 hours at 700°C revealed there was no remaining unreacted iron in the middle of the sample; it had all been converted to an iron silicide.

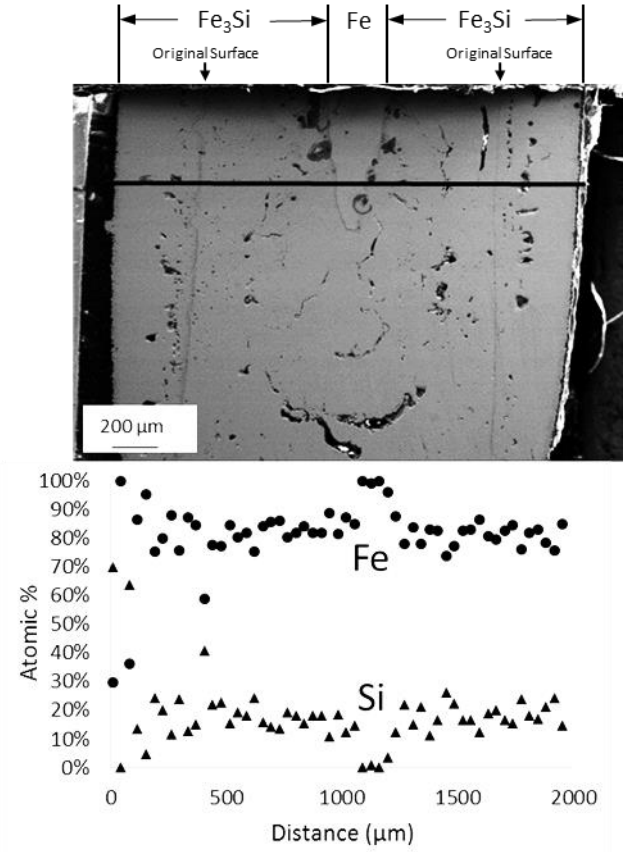

Figure 22: Full width cross sectional image of a sample after exposure to a chlorosilane environment for 100 hours at 650°C. The region in the top middle of the image represents remaining, unreacted iron.

In all samples after exposure at temperatures 600°C and greater, there appears to be two regions of Fe_3Si with the same atomic concentrations. It is proposed that the line separating these two regions marks approximately the location of the original outer edge of the sample. This is due primarily the size of the unreacted samples compared to the spacing of the scars. It could be the result of chlorides evaporating from the surface before a silicide could form. $FeCl_2$ and $FeCl_3$ reach a significant vapor pressure at 536°C and 167°C respectively [21, 55], making 600°C a sufficient temperature for reactive evaporation. This reactive evaporation would potentially leave porosity which is visible

as a scar or line in the cross sections. There are a few reasons that reactive evaporation may leave a scar. The first is due to some non-uniformity of the reactive evaporation as the chloride and silicide species compete for the iron substrate. This may cause an increase in surface roughness at the initial interface. Also, there may be some residual iron chloride trapped on the surface during corrosion exposure that is washed away during the cross sectioning and polishing procedure. This would also result in increased surface roughness at the original interface and porosity that would be visible in cross sectional FEM analysis. However, these hypotheses were not tested for in this study.

A high magnification image of the edge of a cross section of a sample after exposure to 100 hours at 700°C is shown in Figure 23. The EDS line scan shows apparent stratification of iron silicide corrosion layers. When corroborated with XRD, there is substantial evidence of FeSi on the surface of the sample with a sharp transition to Fe_3Si behind it. The FeSi region is darker in the micrograph than the Fe_3Si region making it easy to see. It appears to penetrate more in some areas than others rather than being a flat layer. One explanation is that the surface of the sample is rough and full of nodules as shown in Figure 18. The FeSi layer follows the surface of those nodules, making it appear like it is penetrating deeper in some areas than others. Another explanation is that FeSi grows primarily at the grain boundaries of Fe_3Si. Iron transport is likely fastest at the grain boundaries, making these regions grow faster than other regions. However, it was not confirmed that the areas corresponding to thicker FeSi corresponded to grain boundary locations. Very similar FeSi layers were found on all samples exposed for 100

hours at temperatures greater than or equal to 600°C, with higher temperatures resulting in thicker FeSi layers.

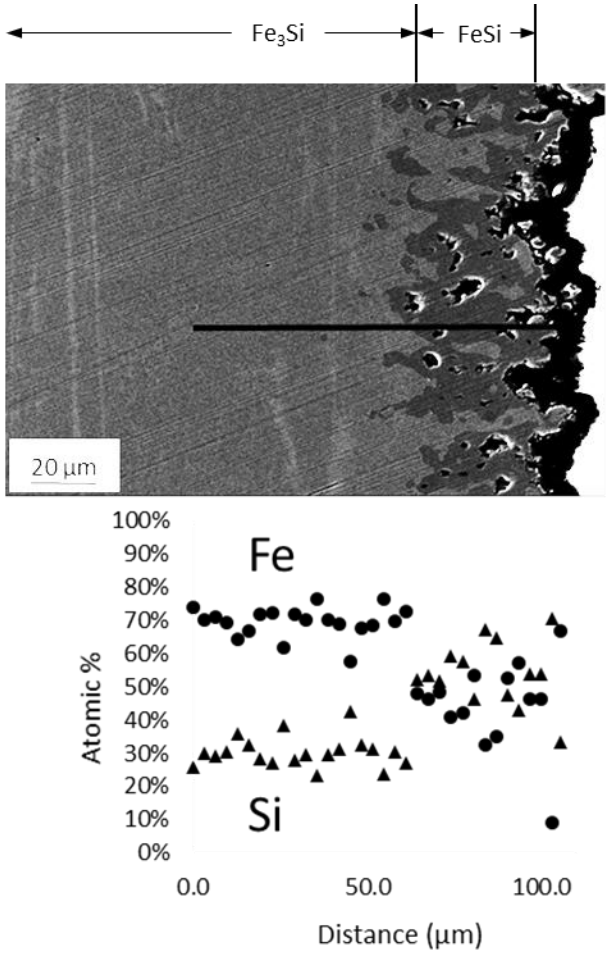

Figure 23: High magnification cross sectional image of a sample after exposure to a chlorosilane environment for 100 hours at 700°C. The dark, FeSi on the surface of the sample was seen on all samples exposed at 600°C and higher.

The layers detected by the cross sectional FEM/EDS were predicted by the predominance diagram shown in Figure 24a. This figure displays the HCl activity on the horizontal axis and the silicon activity on the vertical axis with an iron starting material and a constant temperature and H_2 partial pressure of 600°C and 0.74 respectively. Diagrams at temperatures from 550-700°C have similar shape with slightly different

transition values. This diagram shows that at very low silicon and HCl activity, the iron starting material remains pure iron. This is intuitive and represented by the remaining pure iron in the cross sections of corroded samples. At higher HCl activities and relatively low silicon activity, $FeCl_2$ forms and subsequently vaporizes. At higher Si activity, it takes more HCl to form volatile $FeCl_2$, implying that silicides may impede chloride attack. At increasing Si activity and low HCl activity, the silicide layers get increasingly silicon rich progressing from Fe_3Si to FeSi and $FeSi_2$. This trend was also observed in the analysis with Fe_3Si detected deepest in the bulk and FeSi detected on the surface where the silicon activity is the highest. $FeSi_2$ was not detected in this series of experiments suggesting that either the silicon activity was not high enough to form it, or equilibrium was not yet established.

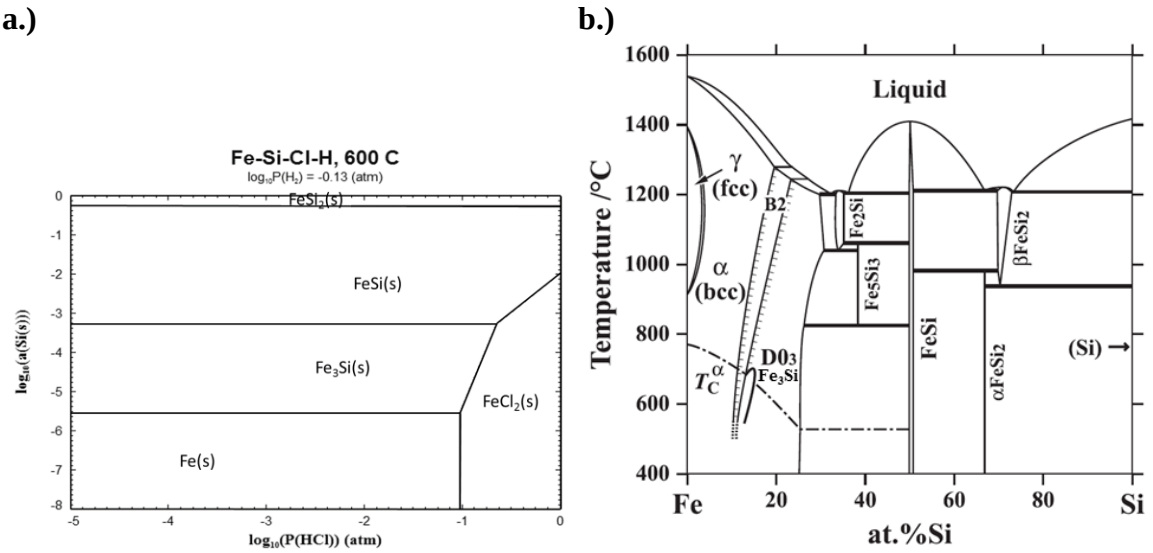

Figure 24: Thermodynamic modeling showing a.) the predominance diagram for the Iron-Silicon-Chlorine-Hydrogen system at 600°C generated by FactSage and b.) the temperature-composition phase diagram for the iron-silicon system calculated by Kubaschewski [56] and regnerated by Ohnuma [57]. In this diagram, T_c^{α} represents the Currie temperature of the alpha (body centered cubic) phase, B2 represents the Cesium Chloride structure of FeSi, and $D0_3$ represents the cubic structure of Fe_3Si.

Complementary to the predominance diagram is the iron-silicon phase diagram shown in Figure 24b. This figure shows that silicon is soluble in iron up to approximately 10 - 12 atomic % between room temperature and 700°C. Fe_3Si exists as a single phase between approximately 12% and 25%, while FeSi is only present as a single phase between 49-51%. In the cross sections analyzed by EDS, there were usually large Fe_3Si layers that had consistent compositions rather than a compositional gradient. Generally this composition was equivalent to stoichiometric Fe_3Si. This is comparable to Zhang and Ivey's work with bulk diffusion couples that showed stoichiometric Fe_3Si is favored and forms more quickly than non-stoichiometric Fe_3Si [32]. There were some cross sections with areas that had a consistent composition with Si content less than that of stoichiometric Fe_3Si. This could be due to a two phase region with the second phase being more iron rich, some unexpected growth of non-stoichiometric Fe_3Si, or error in the quantification of EDS.

Time Dependent Results

The time dependence of the corrosion scale growth was important to explore to understand how the iron silicides form. This series of experiments was run at 600°C with an input mole fraction of 0.74 H_2 and 0.26 STC; the same input stream as the temperature dependent study. These conditions were chosen because they most accurately replicate industrial processes and the temperature dependent study implied that the corrosion layers would form at a reasonable rate. The gravimetric data from these exposures is shown in Figure 25a and the plan view micrographs are shown in Figure 26. Figure 25b also includes transformed gravimetric data that shows the mass change per surface area

plotted against square root of time. This plot shows how well the corrosion complies with parabolic kinetics. The trend line in this plot shows a relatively good fit with parabolic kinetics with the trend starting at roughly 8 hours rather than 0 hours. This may be due to some initial chloride formation and vaporization before a silicide layer can form. Diffusion limited, parabolic growth naturally requires a continuous layer for species to diffuse through. The data suggests that this layer establishes itself after 8 hours in these conditions.

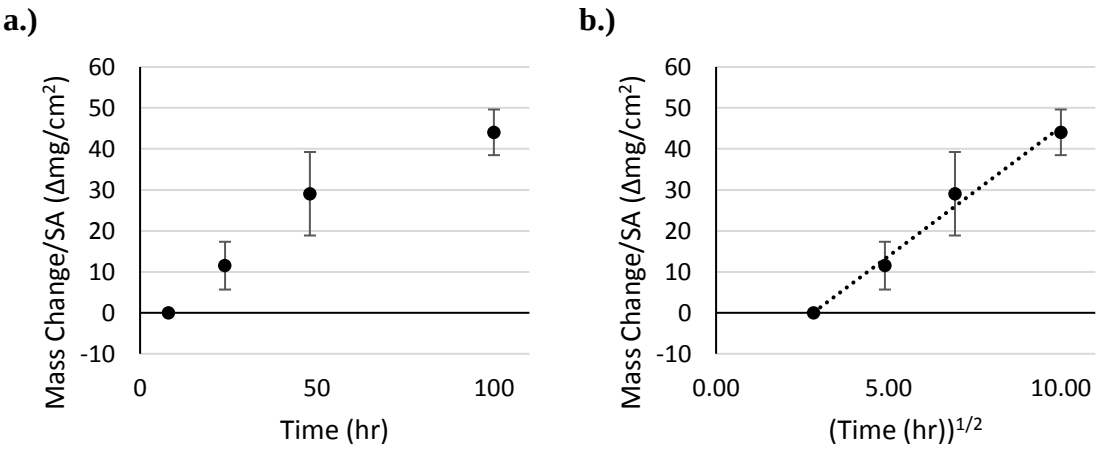

Figure 25: The a) area specific mass change data and b) transformed gravimetric data for the time dependent study. The transformed data plots mass change vs the square root of time to identify if parabolic kinetics are present. The error bars represent a 95% confidence interval on the mean.

The plan view FEM and EDS data supports this theory, with primarily iron being detected after 8 hours, and primarily iron and silicon being detected after 24, 48, and 100 hours. Chlorine was not detected in significant quantities on any of the surfaces, as expected from the high vapor pressure of iron chlorides at 600°C [21, 55]. However, there was substantial evidence for chloride formation in the form of bright yellow iron

chloride in the cool end of the tube furnace. This is likely the result of iron chloride formation and vaporization in the hot zone, followed by condensation after it had cooled. EDS analysis revealed that the collected iron chloride had a composition consistent with $FeCl_2$.

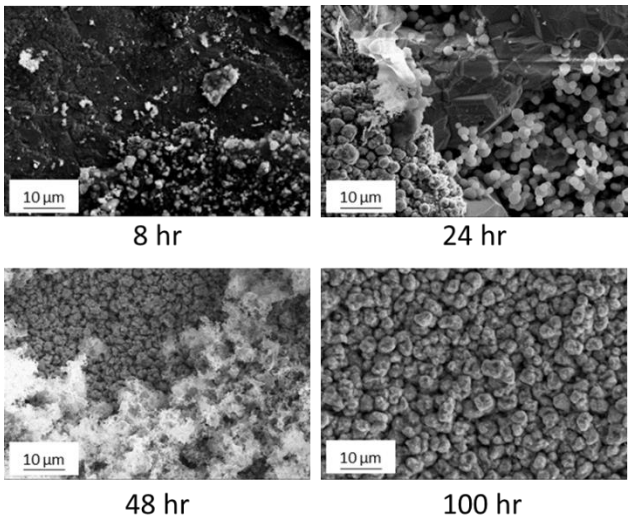

Figure 26: The plan view FEM micrographs for the time dependent study. These samples were exposed to a STC/H2 environment for 8, 24, 48, and 100 hours at 600°C.

Additional information can be garnered from looking at XRD patterns from these samples. A plot of the patterns is displayed in Figure 27. This plot shows from two theta of 40-50 to capture significant Fe, FeSi, and Fe_3Si peaks [47-49]. A scan of the as received iron is displayed first with a peak corresponding to alpha iron. The scan from the sample after 8 hours of exposure also displays a peak near the location of alpha iron and a peak that corresponds to Fe_3Si. The iron peak is shifted slightly to a higher two theta, likely due to silicon substituting into an iron lattice, making the lattice parameters slightly smaller [50-53]. XRD analysis after 24 hours of exposures shows little to no iron on the

surface, and primarily detected FeSi and Fe_3Si. This trend continued at 48 and 100 hours of exposure.

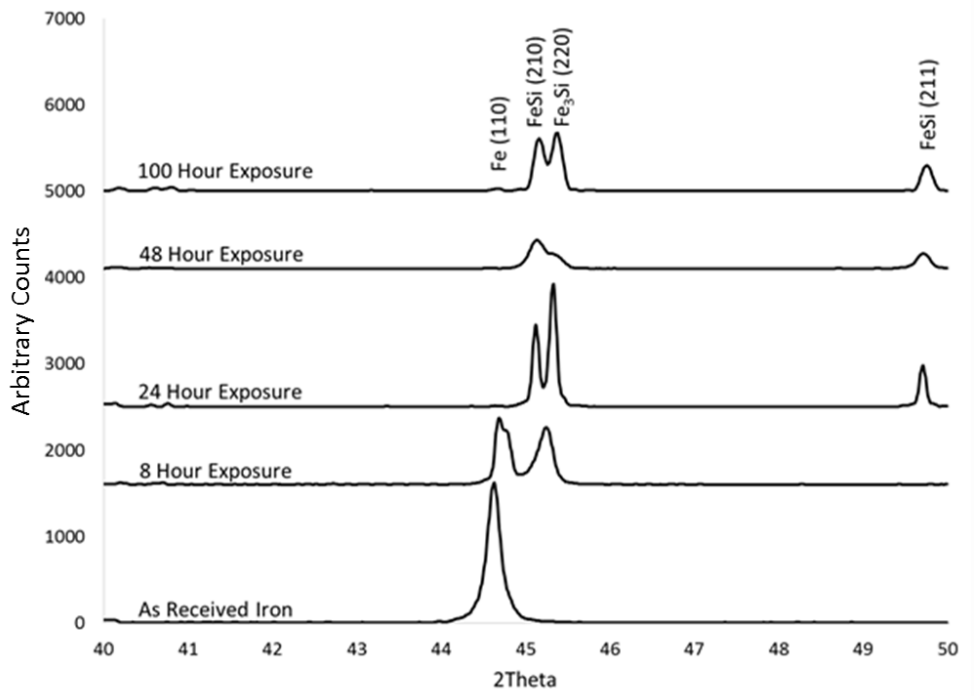

Figure 27: The XRD patterns for iron samples after exposure to chlorosilane environments at 600°C for 8, 24, 48, and 100 hours.

Cross section analysis was used to complement the XRD data. The cross section of the sample after 8 hours of exposure is shown in Figure 28. This shows a large amount of silicon on the surface of the sample that tapers off deeper in the sample. The total depth of silicon penetration is approximately 4 µm. The concentration of silicon is similar to that of stoichiometric Fe_3Si near the surface and less than the solubility limit of silicon in iron (approximately 12 atomic % [56]) deeper in the bulk. This agrees well with the XRD data.

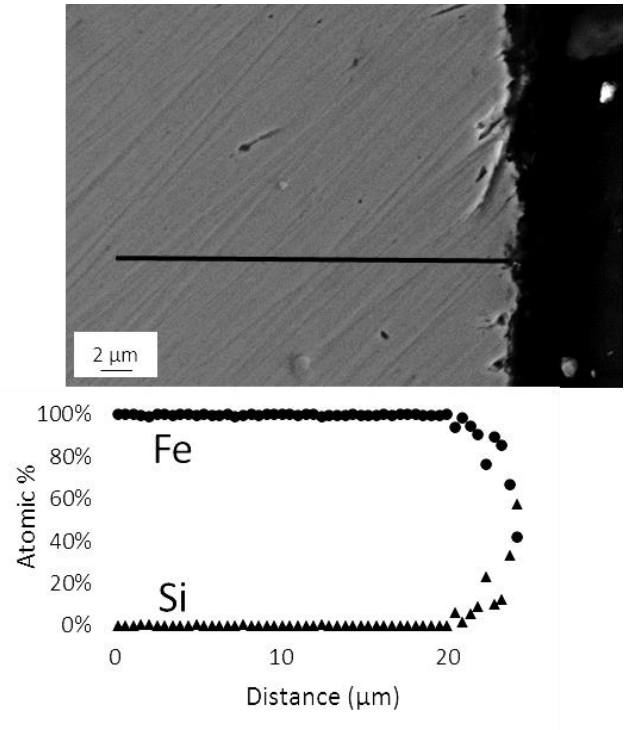

Figure 28: High magnification cross sectional image of a sample after exposure to a chlorosilane environment for 8 hours at 600°C.

A cross section of a sample after 24 hours at 600°C is shown in Figure 29. In this cross section, there is a much larger region similar in composition to Fe_3Si before a similar silicon composition taper to zero atomic %. Again, this agrees with the XRD data that shows primarily Fe_3Si after 24 hours. XRD also indicated FeSi after 24 hours, which was detected with EDS at a higher magnification.

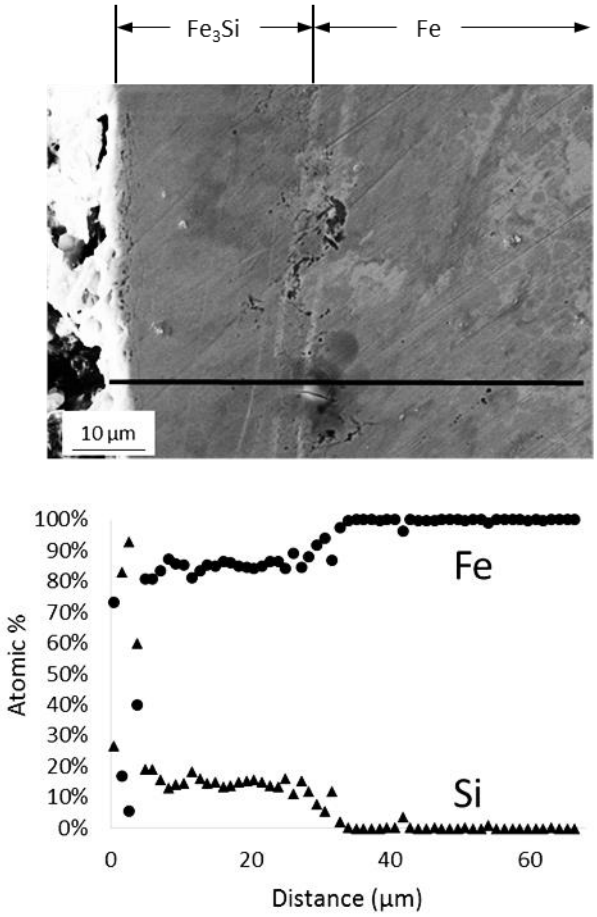

Figure 29: High magnification cross sectional image of a sample after exposure to a chlorosilane environment for 24 hours at 600°C.

Figure 30 shows the cross section and line scan of a sample after exposure at 600°C for 100 hours. This line scan shows stoichiometric FeSi compositions near the surface, a very large region of stoichiometric Fe_3Si, and then the silicon concentration tapers to pure iron. The presence of a FeSi layer was confirmed with a higher magnification image and line scan that was similar in character to Figure 23.

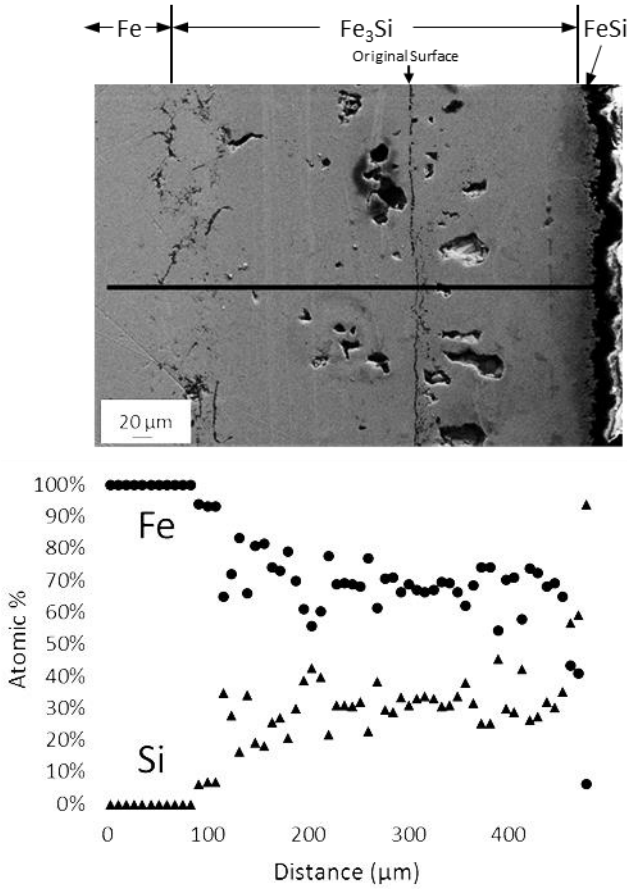

Figure 30: High magnification cross sectional image of a sample after exposure to a chlorosilane environment for 100 hours at 600°C.

Similar to the temperature dependent results, these time dependent results can be confirmed by comparing the stratification to the predominance diagram and phase diagram in Figure 24. However, it is important to remember that these diagrams are based solely on thermodynamics and not kinetics. Therefore, they do not predict what layers may form first.

Discussion of Iron Chlorosilane Corrosion

It appears from the temperature dependent study that the corrosion mechanisms are similar for exposure at temperatures greater than or equal to 600°C. Therefore, this discussion will primarily focus on the formation and progression of iron silicide corrosion layers at or above that temperature. A diagram showing the proposed mechanisms of corrosion is displayed in Figure 31. The first step in this process is silicon deposition. In the figure, it is shown as the direct reaction of silicon tetrachloride with hydrogen to form silicon and hydrogen chloride. It is likely that there are some intermediate gas phase reactions including the formation of trichlorosilane [10, 13] or $SiCl_2$ [30]. However, the end result of these gas phase reactions is suggested to be silicon deposition and adsorption onto the iron surface. An alternative to silicon deposition and adsorption is the direct reaction of chlorosilane species with the iron to form iron silicides. This reaction is likely not the dominate mechanism due to the detection of substitutional silicon in an iron lattice prior to iron silicide formation.

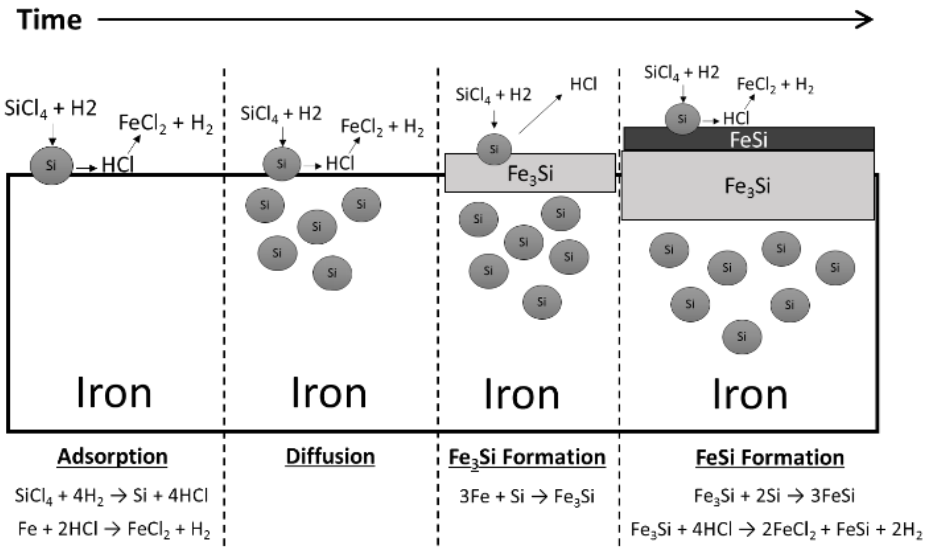

Figure 31: Proposed corrosion behavior of iron in chlorosilane environments between 600 and 700°C.

The hydrogen chloride produced as a result of this silicon deposition very likely reacts with iron forming volatile iron chloride. This is shown in Figure 31 as $FeCl_2$ formation, however $FeCl_3$ is also possible. Once the silicon is deposited on the iron, it starts to diffuse into the iron. Once there is a high enough concentration of silicon on the surface, it reacts with the iron to form Fe_3Si. The data after 8 hours of exposure reflects roughly this time period. At this point, there is a thin layer of Fe_3Si, some iron saturated with silicon, and a taper of silicon concentration in the iron. The slight mass loss of these samples is also representative of iron chloride formation and evaporation. The next step in the corrosion process involves Fe_3Si growth and FeSi formation. FeSi can form from either the reaction of deposited Si with Fe_3Si or the reaction of Fe_3Si with HCl. These reactions are both displayed in Figure 31. Both cases have been reported in the literature [31, 39], and it is likely that both reactions happen simultaneously. This stage is represented by the data after 24 hours. At this point there is a thin FeSi layer, a large

section of Fe_3Si, and finally a taper of silicon concentration in the iron. For longer periods of time, it appears that both the Fe_3Si and FeSi continue to grow. At some point, there may be a high enough silicon activity to form $FeSi_2$, but it was not observed in this series of tests.

Previous Mossberg spectroscopy [58] and tracer diffusion investigations [59] have reported that iron diffusion in Fe_3Si is quite fast while silicon diffusion is slow. This indicates that Fe_3Si formation occurs at the Fe_3Si-FeSi interface. Additionally, iron diffusion has been reported as the dominate transport mechanism in FeSi [60]. However, iron diffusion is much faster in Fe_3Si than FeSi. This is potentially the reason Fe_3Si scales are much thicker than FeSi scales. An analog to this situation is the layered formation of iron oxides; wüstite, magnetite, and hematite. Wüstite layers are often much thicker than magnetite and hematite layers due to the high iron and oxygen self-diffusion coefficients [61]. Future work could verify this assumption.

Additional future work in the field of silicide and chloride formation is to quantify the amount of iron chloride volatilization via precise gravimetric data and corrosion scale thickness and density measurements. If one knew the density and thickness of the silicide scale, the theoretical mass change from silicide formation could be calculated. Deviations from this theoretical mass change could then be related to chloride formation. Then, the establishment of long term paralinear kinetics could be assessed; similar to the work of Maloney and McNallan [62]. However, in this experiment, this calculation could not be done accurately due to bulk silicide layer density variations from a significant amount of

porosity, variations in corrosion layer thickness, and significant edge effects due to the relative size of the corrosion scale compared to the original sample.

Another consideration when evaluating this model are the effects of grain boundaries on diffusion, Fe_3Si formation, and FeSi formation. Diffusion is known to primarily occur in grain boundaries, indicating that the silicon activity will be higher in the grain boundaries than it is in the centers of the grains. This means that Fe_3Si and FeSi will form at the grains before they form in the bulk crystals. This may be why FeSi appears to penetrate deeper into the Fe_3Si in some places than others as seen in Figure 23. These areas of high penetration likely correspond to grain boundaries in the Fe_3Si. This effect has been previously reported by Rebhan, et al [29].

Figure 31 represents the first time a mechanism of iron corrosion in chlorosilane environments has been proposed. This is significant because understanding how a metal corrodes in a specific environment is the first step in understanding how to protect it from that environment. If any step in the corrosion process can be cut off by alloying or other means, it will prevent the iron from further corrosion and allow for use of low cost iron based alloys in chlorosilane applications. For example, if an alloying element can be added to the iron to reduce the silicon diffusion into the iron lattice, it would impede the formation of Fe_3Si and FeSi, making the corrosion process less detrimental. This may have been the case in the previous study on chlorosilane corrosion of AISI 316L [43]. In that study, the 316L corroded approximately $1/8^{th}$ as much as iron in similar conditions as measured by mass change per surface area. This is potentially due to the alloying

elements present in 316L such as chromium and nickel impeding silcidation. However, further investigation needs to be done in the field to confirm this assertion.

Conclusions from Iron Chlorosilane Corrosion Study

In this study, pure iron was exposed to a hydrogen/STC environment at a variety of times (8-100 hours) and temperatures (550-700°C) relevant for understanding the corrosion mechanisms at play. It was discovered that exposures for 100 hours at temperatures between 600 and 700°C resulted in similar mechanisms as indicated by transformed gravimetric data, XRD patterns, and plan view and cross sectional FEM/EDS. These exposures all resulted in thick Fe_3Si layers beneath thinner surface FeSi layers. The higher temperature increased the thickness of these layers to the point where there was no remaining pure iron after the 700°C run. The exposure at 550°C resulted in markedly different corrosion products including a different phase of Fe_3Si.

A time dependent study was also conducted at 600°C exposures. In this study, it was discovered that parabolic kinetics exist after an initial scale can be formed. A proposed mechanism for iron silicide formation in chlorosilane environments includes silicon deposition and surface adsorption, silicon diffusion in to the iron lattice, Fe_3Si formation, and FeSi formation. Further understanding of each of these mechanisms and how to prevent them will result in implementation of low cost iron based alloys in chlorosilane service.

INFLUENCE OF SILICON ON THE CHLOROSILANE CORROSION OF IRON

Previous work on the chlorosilane corrosion of iron investigated the corrosion mechanisms present when pure iron was exposed to an input stream of 0.74 mole fraction H_2 and 0.26 mole fraction STC. This work was important because it laid the framework for understanding the corrosion mechanisms at play when iron is exposed to this type of environment. However, many chlorosilane environments take place in the presence of silicon which can alter the gas composition. The purpose of this study was to investigate the corrosion behavior in these altered environments. This work was published in *Solar Energy Materials and Solar Cells* [63].

Corrosion Environment Introduction

Like many gas mixtures, the composition of a chlorosilane mixture changes dramatically when it is heated from room temperature to high temperatures seen in industry (approximately 600°C). For example, a STC/H_2 input stream may form significant amounts of TCS, DCS, and HCl when it is heated. The presence of materials that can vaporize into the gas stream further complicates these reactions. The most common material added to a chlorosilane gas stream is silicon. Silicon may be present in a fluidized bed reactor used to convert silicon tetrachloride to trichlorosilane or deposition equipment used to deposit silicon on a wafer. In each case, the reactor's material of construction must be able to withstand the new environment created by the STC/H_2/Si mixture at high temperatures. This study investigates the corrosion behavior of iron in these environments.

The procedure for exposing iron samples to an altered chlorosilane environment is very similar to the procedure for previous studies. The primary difference in this work compared to previous work was the addition of granular metallurgical grade silicon (MG-Si) to the tubular crucible. Figure 32 shows the general layout of the inside of the tube furnace with the additional MG-Si surrounding the first three samples and held in place by loosely packed quartz wool that allowed gas to flow through it. These samples are referred to as “in pack”. One “out of pack” sample was placed immediately after the quartz wool downstream of the MG-Si. Only one sample was used here due to space constraints. Samples run in exposures without any MG-Si present are referred to as “no pack”. Additionally, some runs were performed with samples “in pack” with a 5% hydrogen 95% argon gas input mixture. The purpose of these runs in a reducing environment were to study the effect of pure silicon diffusion into the iron. These runs will be referred to as "reducing diffusion".

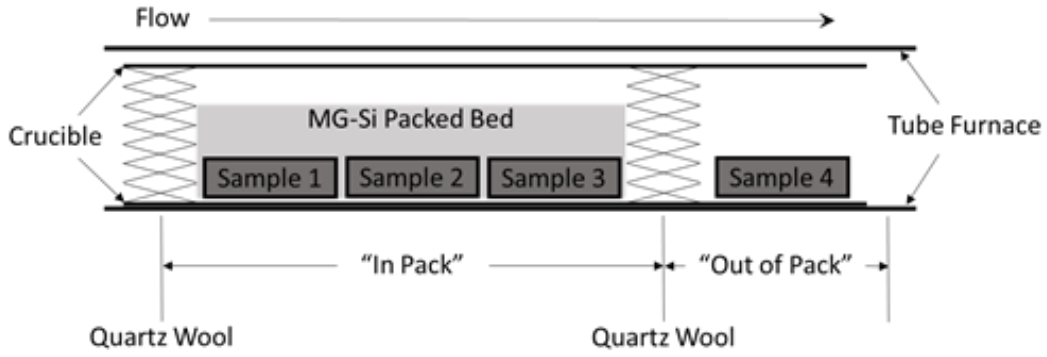

Figure 32: Cross sectional diagram showing the layout of the tube furnace used for chlorosilane exposure and the terminology used to describe the location of samples.

The iron used in this experiment was 99.6% pure with weight percent impurities of 0.025 carbon, 0.03 chromium, 0.04 copper, 0.18 manganese, 0.05 nickel, 0.012

phosphorous, 0.025 sulfur, and 0.05 silicon. Samples were cut to approximately 12 mm x 12 mm x 1.5 mm, deburred, and rinsed with isopropanol and water. Sample surfaces had a 1200 grit finish prior to exposure. The MG-Si had an approximate average particle size of 100-400 μm prior to exposure. EDS was performed on the MG-Si as received, and no impurities were detected. However, it is very likely that there are many impurities present that were below the detectable limits of EDS without standards. Common impurities in MG-Si are iron, copper, nickel, arsenic, aluminum, phosphorous, and boron. These impurities are also known to catalyze the STC to TCS conversion reaction [18].

Iron Packed Bed Exposure Results

Figure 33a shows the plot of specific mass change against time for the "in pack" and "out of pack" conditions. Also included for comparison are the results from the "no pack" study. Figure 33b shows this same data on transformed axes to display the fit with parabolic kinetics. This plot shows that the "in pack" and "out of pack" data closely follows parabolic kinetics, even at the shortest time interval of 3 hours. The "in pack" error bars represent a 95% confidence interval. These error bars are fairly small compared to “no pack” error bars, indicating the samples were exposed to a very consistent atmosphere. There are no error bars on the "out of pack" data because there was only one "out of pack" sample per run. Figures 33a and 33b also show the mass data for “in pack” samples that were only exposed to a reducing environment, not a H_2/STC environment. These runs were performed to measure the influence of silicon diffusion into iron at these temperatures. The reducing environment was required to prevent silicon or iron

oxidation. As is shown in the plot, the influence of diffusion is minor as there is near-negligible mass change to the iron samples after 100 hours at 600°C. This result is consistent with previous diffusion studies [31].

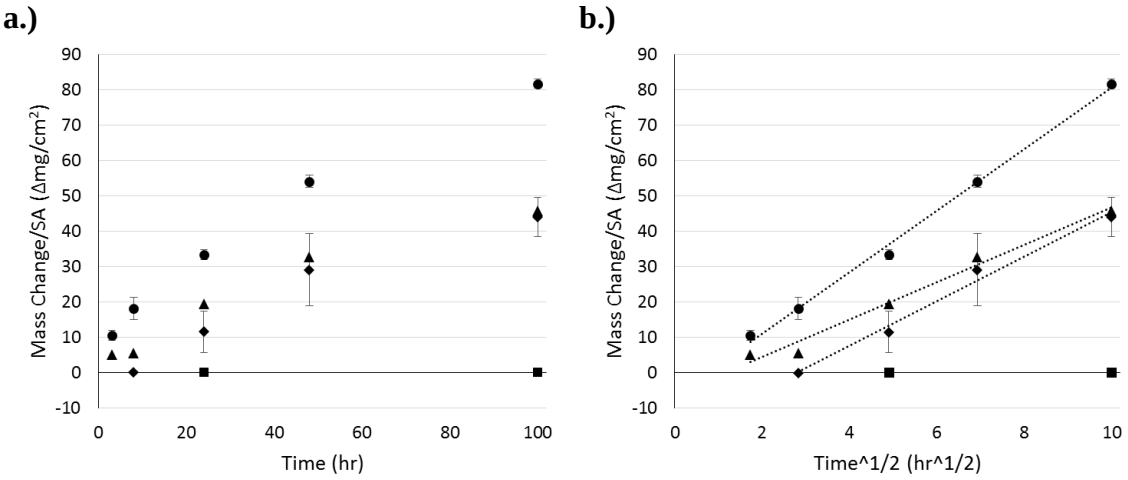

Figure 33: The specific mass change plotted against a.) time and b.) square root of time for samples ● in pack; ▲ out of pack; ◆ no pack; ■ reducing diffusion. Where present, the error bars represent a 95% confidence interval on the mean.

Figure 34 shows the plan view FEM micrographs for the "in pack" samples after various time intervals. These images show fairly consistent surface topography at the various time intervals. The main difference between time intervals seems to be the larger nodules at longer times.

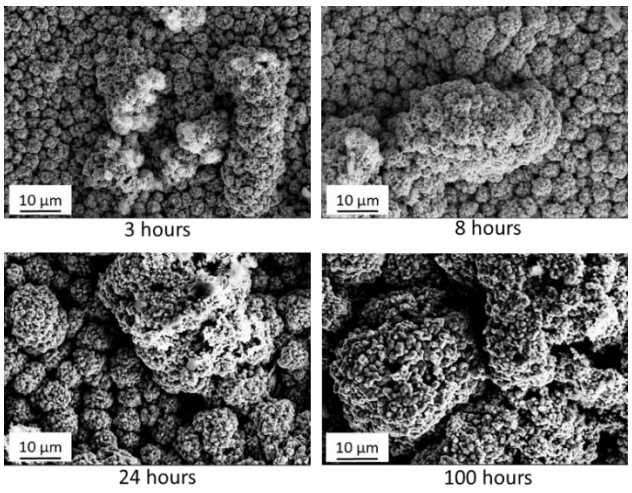

Figure 34: Plan view FEM images of “in pack” samples exposed for a variety of times at 600°C.

Figure 35 shows the FEM micrographs for the "out of pack" samples. Similar to the “in pack” samples, the main result is that longer exposure times resulted in larger nodules on the surface. Comparing “in pack” to “out of pack” samples shows that “in pack” samples have consistently larger nodules for a consistent time exposure. EDS analysis showed surface compositions consistent with stoichiometric FeSi for all samples.

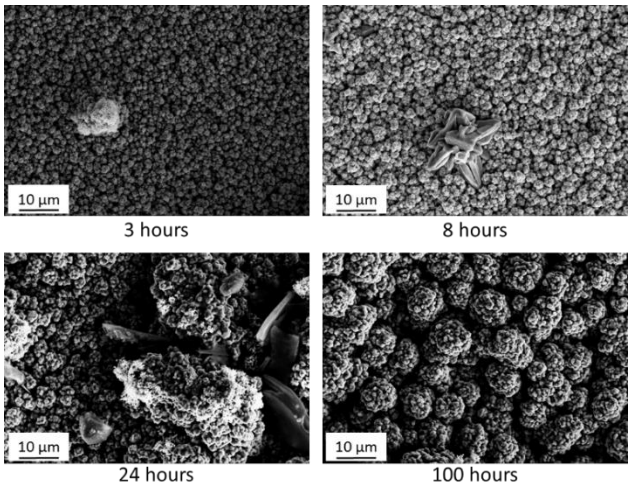

Figure 35: Plan view FEM images of “out of pack” samples exposed for a variety of times at 600°C.

XRD patterns were collected for 2 Theta equaling 15-70 degrees. The patterns between 40 and 50 degrees are shown for "in pack" and "out of pack" samples in Figure 36a and Figure 36b respectively. The range of 40-50 degrees was selected because it encompassed all major peaks of interest [47-49]. It appears from these patterns that there was no detectable alpha (BCC) iron within the interaction volume of the XRD analysis for any of the exposed samples. This is significant because it implies that there is a relatively thick corrosion layer on the surface of the samples that covers any remaining pure iron in the middle. Figure 36a shows that for “in pack” samples, primarily FeSi was detected after all time intervals. There was some Fe_3Si present, but it is relatively small compared to FeSi. Figure 36b shows that for “out of pack” samples, there is primarily Fe_3Si after three hours, but that transitions to primarily FeSi at longer time intervals. After all time intervals, there was more FeSi on the “in pack” samples compared to the “out of pack” samples. This indicates a thicker FeSi layer on the “in pack” samples that more completely covers the Fe_3Si layer compared to “out of pack” samples.

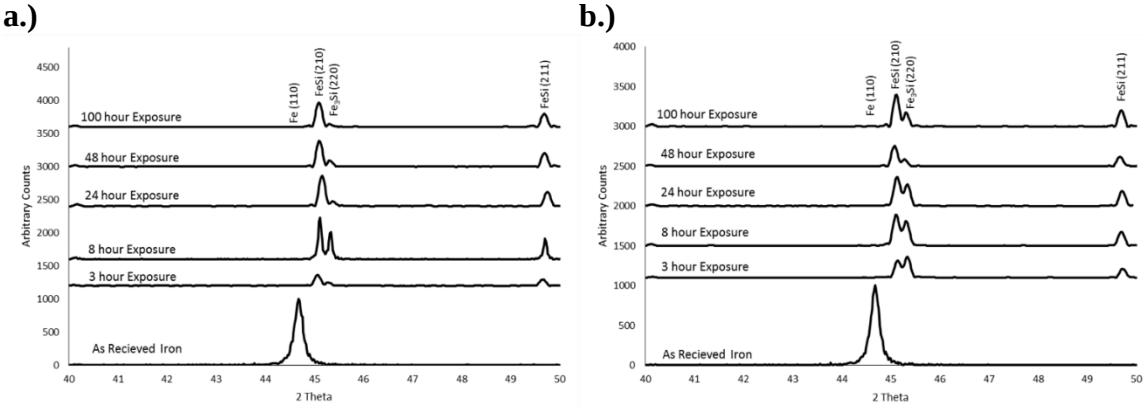

Figure 36: XRD patterns of a.) “in pack” and b.) “out of pack” samples after a variety of times at 600°C exposures. Peaks are labeled according to identification with Jade software.

Cross sectional analysis was able to confirm this claim. Figure 37 shows the full width cross section of an "in pack" sample after 100 hours of exposure at 600°C. The EDS line scan shows an iron and silicon containing layer approximately 600-700 µm thick. The atomic concentrations are consistent with stoichiometric Fe_3Si that was detected with XRD. The interface between the unreacted iron and Fe_3Si region appears to be a gradual decrease in Si concentration rather than a step decrease.

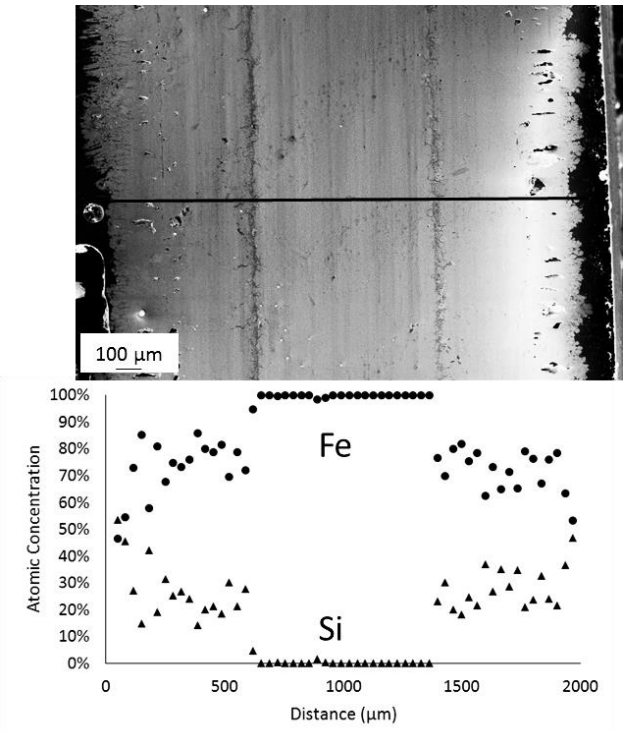

Figure 37: Full width cross section and EDS line scan of “in pack” sample exposed for 100 hours at 600°C.

A higher magnification image of the edge of this sample is shown in Figure 38. The EDS line scan associated with this image shows atomic concentrations consistent with a FeSi region approximately 150 µm thick on top of the Fe_3Si layer. Both the FeSi and Fe_3Si layers appear to be quite dense with only minor amounts of porosity. The

surface of the sample (edge of the cross section) is very jagged with sharp peaks emerging from the bulk.

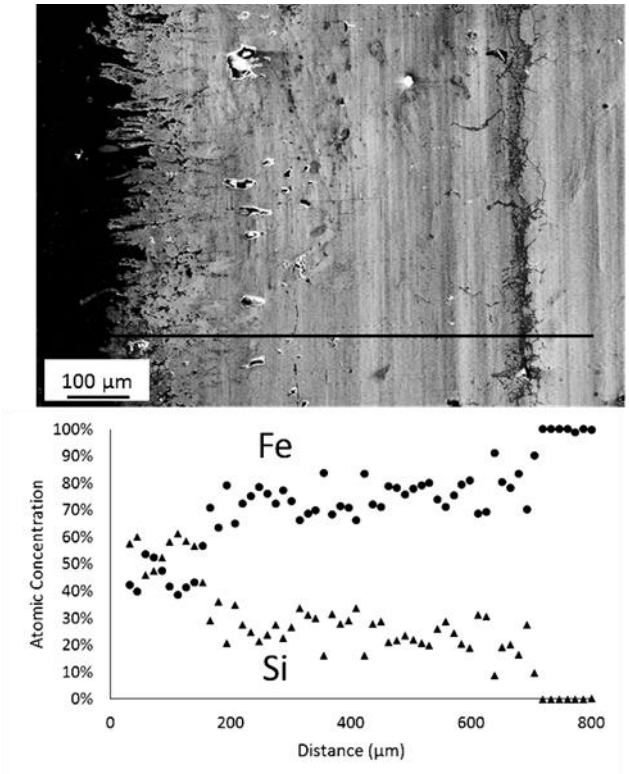

Figure 38: High magnification image and EDS line scan of “in pack” sample exposed for 100 hours at 600°C.

Figure 39 shows the full width cross section of an "out of pack" sample after 100 hours at 600°C. This sample has a similar structure to the "in pack" sample, but with a much thinner corrosion layer. The Fe_3Si layer in this sample was approximately 350 µm thick.

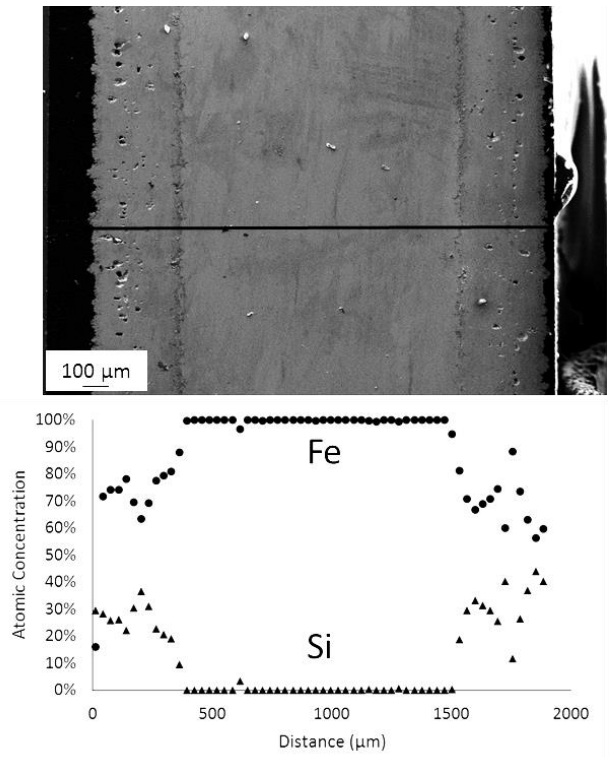

Figure 39: Full width cross section and EDS line scan of “out of pack” sample exposed for 100 hours at 600°C.

Figure 40 shows a higher magnification image of the same sample, and the FeSi layer in this sample appears to be only approximately 20 µm thick. The corrosion layer for this "out of pack" sample has slightly more porosity than the "in pack" sample, but it is still relatively dense.

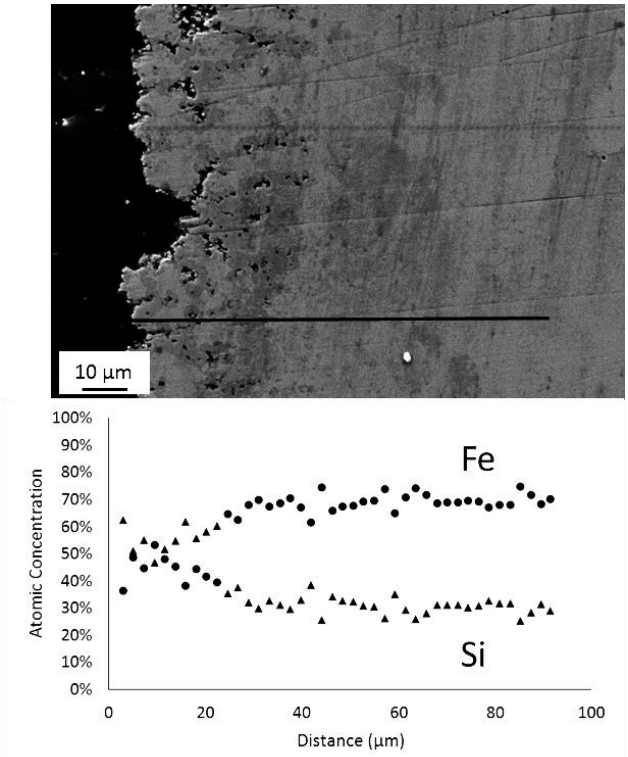

Figure 40: High magnification image and EDS line scan of "out of pack" sample exposed for 100 hours at 600°C.

Figure 41 shows the cross section of an "in pack" iron sample exposed for 8 hours. This image shows a similar transition from pure iron to stoichiometric Fe_3Si. It also appears to show a transition from Fe_3Si to FeSi.

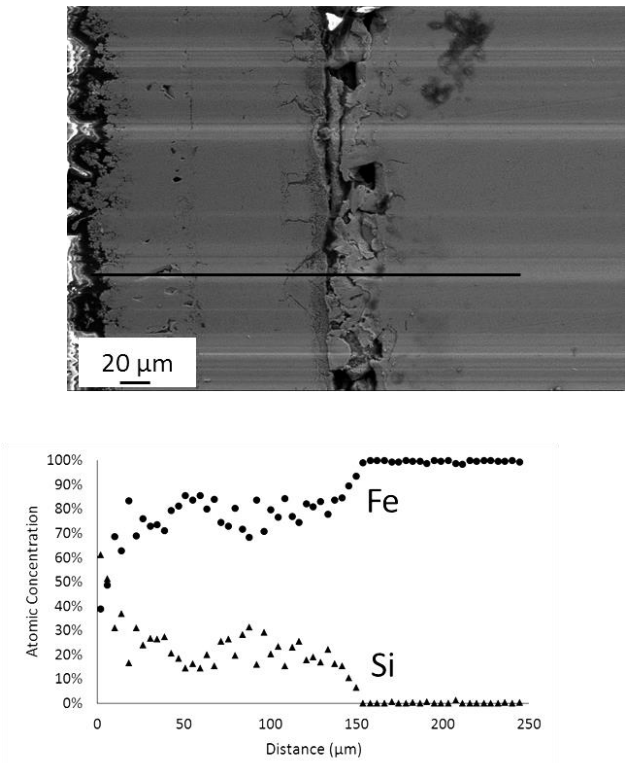

Figure 41: FEM image and EDS line scan of "in pack" sample exposed for 8 hours at 600°C.

To confirm this, a higher magnification cross section is shown in Figure 42. This figure clearly shows a layer of stoichiometric FeSi followed by a layer of Fe_3Si. The FeSi layer is approximately 14 µm thick and the Fe_3Si layer is approximately 140 µm thick, which is significant for only 8 hours of exposure.

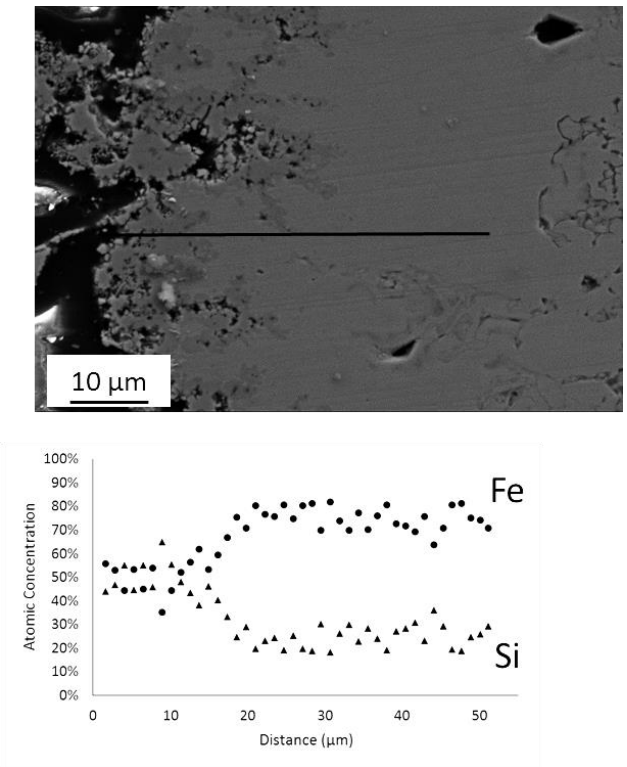

Figure 42: High magnification image and EDS line scan of "in pack" sample exposed for 8 hours at 600°C.

A comparable "out of pack" sample is shown in Figure 43. This figure shows a much thinner Fe_3Si layer compared to the "in pack" sample, equaling only approximately 50 µm. A high magnification line scan of this sample revealed a FeSi layer approximately 8 µm thick, also much thinner than the comparable "in pack" sample. A comparison of Figure 42 and Figure 43 also reveals significantly more porosity in the "out of pack" sample, a trend also seen in the 100 hour exposure.

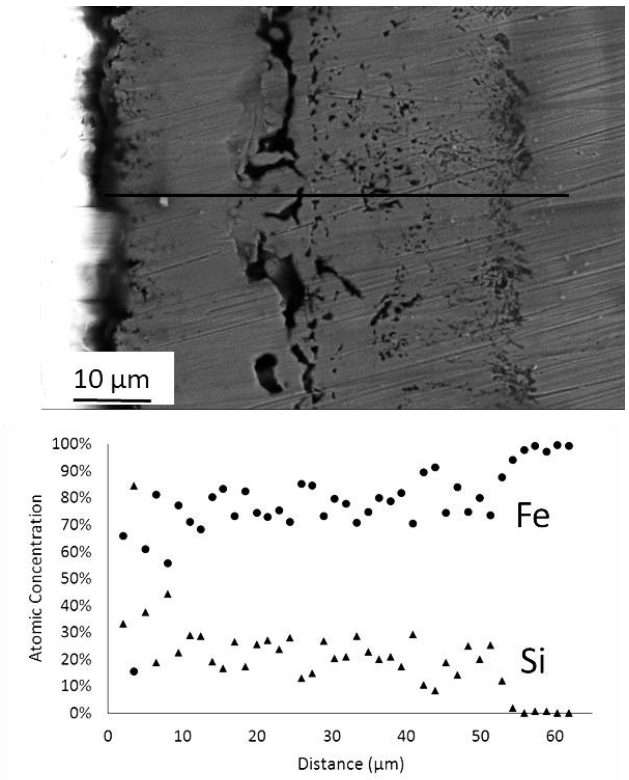

Figure 43: High magnification image and EDS line scan of "out of pack" sample exposed for 8 hours at 600°C.

Iron Packed Bed Exposure Discussion

It is clear that embedding iron samples in metallurgical grade silicon increases the iron silicide layer thickness formed from an STC/H_2 input stream. However, it is likely that this increase is not due to significant solid diffusion of silicon into the iron. This is because the iron samples gained essentially zero mass and had no surface chemistry changes when they were exposed to a reducing environment while embedded in MG-Si. Therefore, it is likely that the MG-Si reacted with the chlorosilane gas at 600°C to form a gas phase with a higher silicon activity. FactSage thermochemical software with FactPS 7.0 database was used to calculate chemical equilibrium for several cases to help explain

the higher silicon activity [64]. The results are displayed in Table 3. The lower cutoff limit for all species was 1.0E-10 mole fraction. A fixed mole fraction of 0.74 H_2 and 0.26 STC was used to represent a tube furnace where reactants are constantly being added to the mixture. The first calculation allowed these reactants to reach equilibrium at 600°C without additional silicon. This calculation revealed that many other species form at equilibrium including HCl, TCS, and DCS. This represents the "no pack" scenario reported previously in the literature. At equilibrium, this mixture has a silicon activity of 0.00184.

The next calculations included fixed silicon content to simulate the presence of MG-Si. At equilibrium, it doesn't matter how much silicon started in the system because it will all react with the flowing H_2 and STC. Comparing the equilibrium simulations with and without silicon indicates that the additional silicon has significant influence on the gas phase equilibrium. In the simulation with additional Si, there is significantly more TCS and DCS with less HCl compared to the simulation without additional Si. Also, the silicon activity for the simulation with additional Si is 0.547, over two orders of magnitude higher than the calculated Si activity without silicon (0.00184). This represents the gas environment experienced by the "in pack" samples in this study.

Equilibrium Mole Fractions at 600°C Room Temperature Input: Fixed 0.74 H_2 /0.26 STC			
	Additional Si		
	None	1 mole Si	100 mole Si
H_2	7.11E-01	6.72E-01	6.72E-01
STC	2.50E-01	2.36E-01	2.36E-01
HCl	1.97E-02	4.06E-03	4.06E-03
TCS	1.94E-02	8.42E-02	8.42E-02
DCS	1.37E-04	2.74E-03	2.74E-03
$SiCl_3$	6.03E-05	2.62E-04	2.62E-04
$SiCl_2$	8.54E-07	1.70E-05	1.70E-05
SiH_3Cl	2.33E-07	2.14E-05	2.14E-05
SiH_4	1.79E-10	7.54E-08	7.54E-08
Si (s) Activity	1.84E-03	5.47E-01	5.47E-01

Table 3. Equilibrium gas composition calculated by FactSage for several cases relevant for chlorosilane corrosion.

There was clear evidence for silicon consumption in the experiment to support the theory that silicon was added to the gas phase. FEM micrographs of the MG-Si before and after exposure are shown in Figure 44. The as-received MG-Si contained granules approximately 100-400 μm in diameter that had relatively smooth edges. The MG-Si after exposure contained significantly smaller granules that were very rough. It also changed from a jet black color as received to a brown color after exposure, potentially due to the changes in surface morphology. The mass of the MG-Si was taken before and after exposure so that the amount of MG-Si consumed could be calculated; the result is shown in Figure 45. This provides evidence of MG-Si reacting in to the gas phase and changing the gas phase composition as predicted.

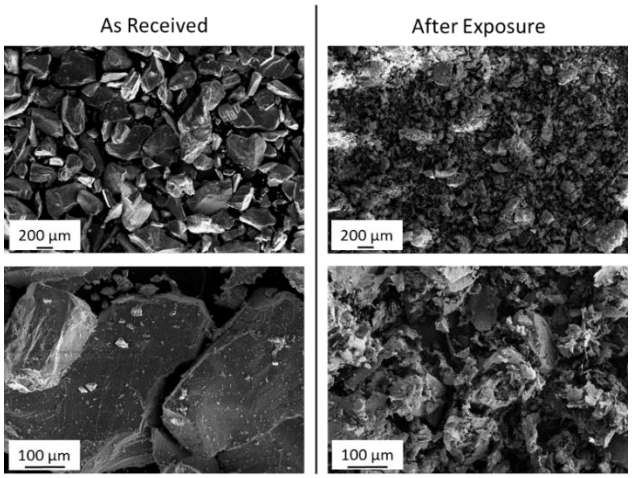

Figure 44: FEM images of MG-Si as received and after 100 hour exposure at 600°C.

Higher silicon activities in the gas phase will correspond with higher silicon activities in the condensed phase. A predominance diagram that relates the iron based condensed phase with silicon and HCl activity is shown in Figure 24. A higher silicon activity corresponds with a more silicon-rich iron silicide. Also, the predominance diagram predicts that a sufficiently high silicon activity will prevent any iron chlorides from forming. Iron chlorides are volatile at 600°C and are often to blame for porosity in corrosion layers [21, 24, 55]. Therefore, the thicker silicon-rich silicide layer and lack of porosity in the "in pack" samples compared to the "no pack" samples are likely due to increased silicon activity. The higher silicon activity also translates to the "out of pack" samples. The "out of pack" case is much more difficult to model thermodynamically. However, some inferences can be made based on the experimental results. The increased porosity and thinner FeSi layers of the "out of pack" samples compared to the "in pack" samples indicates a lower silicon activity for the "out of pack" samples. However, comparison to previously reported "no pack" samples indicates that the silicon activity in the "out of pack" case is higher than "no pack" [46]. This is likely due to the gas

environment becoming more silicon rich as it flows over the packed bed of silicon, and the gas retaining that silicon as it exposes the “out of pack” samples.

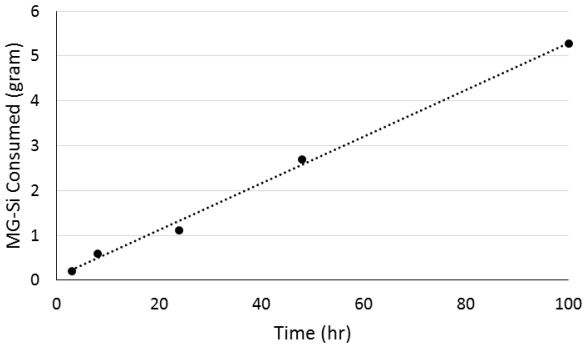

Figure 45. Plot of MG-Si consumed per run time as measured by weighing the MG-Si before and after exposure. The calculated trend line was (MG-Si consumed (gram)) = 0.0522*(Time (hr)) + 0.0692 with an r-squared value of 0.996.

This higher silicon activity has both helpful and harmful effects from a corrosion standpoint. The fact that it decreases or prevents iron chloride formation is helpful because the formation of volatile chlorides consumes the base metal and may lead to decreased metal thickness. However, the formation of silicon-rich iron silicides does not seem to be fully protective. The parabolic kinetics illustrated by the mass data is evident, but the cross sectional analysis shows that a significant amount of base iron has been converted to Fe_3Si or FeSi; both of which have different physical and chemical properties than pure iron.

It is suggested that the mechanisms for corrosion “in pack” are similar to the previously described mechanisms for “out of pack” chlorosilane corrosion with the primary difference being the higher silicon activity. The higher silicon activity in the gas phase corresponds to a higher silicon activity on the surface of the iron, which increases

the chemical potential gradient or concentration gradient which is the diffusion driving force according to Fick's Law. The increased driving force increases the rate of corrosion, but it is likely that the mechanisms of silicon adsorption, diffusion, and silicide formation remain the same.

Iron Packed Bed Conclusions

This study investigates the chlorosilane corrosion behavior of pure iron and the influence of a packed bed of silicon at various time intervals and 600°C. It was discovered that stratified surface layers of FeSi and Fe_3Si form very quickly in these conditions, and parabolic kinetics are established after just 3 hours of exposure. FEM, EDS, and XRD were employed to confirm the presence of FeSi and Fe_3Si and their location relative to the base metal. The corrosion layers of "in pack" samples were significantly thicker than "out of pack" samples, likely due to the higher silicon activity in the pack. Additionally, there was less evidence of chloride formation on the "in pack" samples as seen by the lack of porosity. Comparison to previously reported predominance diagrams show that the lack of chloride formation is also likely from the increased silicon activity.

Thermochemical modeling was used to show the effect of MG-Si on the equilibrium composition of an input stream of STC and H_2. This modeling revealed an equilibrium silicon activity two orders of magnitude higher for the "in pack" case compared to "no pack". This increased gas phase silicon activity is due to solid silicon consumption, a claim confirmed by weighing and imaging the packed bed of MG-Si

before and after exposure. Additionally, the implications of a higher silicon activity and the corrosion layers formed because of it were discussed. The results of this study show the importance of replicating a chlorosilane environment as precisely as possible to get appropriate corrosion data.

GENERAL CONCLUSIONS AND FUTURE WORK

The first part of this work included the corrosion exposure of AISI 316L to high temperature chlorosilane environments. The purpose of this study was to test the implications of using a low cost stainless steel in high temperature chlorosilane applications, and determine the implications of changing the temperature, HCl content, and time of exposure. The study found that without HCl in the input at 550°C, primarily silicon containing corrosion scales were formed. With increasing HCl, there were more chlorine containing corrosion products and fewer silicon containing corrosion products. This trend continued until there were only chlorine containing corrosion products. This trend of increased HCl corresponding to increased chlorine corrosion products was not seen at higher temperatures; a phenomenon supported by thermochemical data. In primarily silicide forming conditions, the corrosion scale growth was parabolic implying that the scale is protective. At lower temperatures, there was evidence for reaction limited growth.

In order to conduct a more fundamental study, pure iron was exposed to a variety of chlorosilane environments. Iron was found to exhibit parabolic silicide forming behavior after an initial chloride forming period. The iron silicides formed from these exposures were stratified with a thin layer of FeSi on the surface, a thick Fe_3Si region next, and finally, silicon diffused into an iron lattice resulting in a silicon concentration gradient. A proposed mechanism of iron silicide growth in these environments from 600-700°C included silicon deposition and adsorption onto the iron surface, silicon diffusion into the iron lattice, Fe_3Si formation, and FeSi formation. It was suggested that

eliminating any of these steps by alloying or other means will significantly decrease the rate of silicide formation and decrease corrosion. Comparing similar results of AISI 316L to pure iron reveals that the pure iron gained approximate 8 times as much mass as AISI 316L in similar environments.

In order to more closely replicate industrial processes, the next study focused on the influence of metallurgical grade silicon on iron chlorosilane corrosion. The addition of metallurgical grade silicon significantly increased the silicide formation rates in iron compared to similar conditions without metallurgical grade silicon. It was suggested that metallurgical grade silicon increased the silicon activity of the gas phase due its reaction with the input gas species. This claim was supported by surface analysis of the metallurgical grade silicon before and after exposure and thermochemical modeling of the system. The increased silicon activity decreased the porosity that was observed in the corrosion surface layers. This was likely due to decreased chloride formation.

Comparing the results of these three studies leads to several conclusions on the corrosion mechanisms of low cost metals in chlorosilane environments. First, it is important to note that metals can indeed form either predominately metal chlorides or metal silicides depending on the silicon activity, the chlorine activity, and the temperature of exposure. There are several ways to change the silicon and chlorine activity in a chlorosilane environment. Adding metallurgical grade silicon was shown to increase the gas phase silicon activity while adding hydrogen chloride was shown to increase the chlorine activity. The increased silicon activity decreased the chloride formation as was shown by the lack porosity in the corrosion layer. The increased chlorine activity by HCl

addition was demonstrated by sample mass loss due to the formation of volatile chlorides. These phenomena and trends were compared to thermodynamically generated predominance diagrams and chemical equilibrium calculations, which confirmed the correlation with theory.

Future work in this field could further investigate the reasons why AISI 316L corroded so much less than pure iron. It is possible that it is due to the addition of major alloying elements such as nickel and chromium, but it could also be due to minor alloying elements or the presence of the austenitic phase. A series of tests that varies the composition and phase of several stainless steels would provide a better understanding as to what is required to prevent chlorosilane corrosion. The effect of surface engineering could also be studied in this corrosion testing system. Coatings to protect the base metal could be tested and implemented, allowing industrial users to implement low cost alloys with a corrosion resistant coating. Additional future work could include further understanding the environment created by the packed bed of MG-Si. It is clear that this packed bed has a substantial influence on the corrosion environment, but it is unclear exactly what the gas composition over the samples is. Further understanding of this environment would ensure that the experimental setup is imitating industrial systems as closely as possible.

Additional future work includes looking mechanistically at the formation of iron silicides in these environments. Exposing single crystal iron to chlorosilane environments would allow for a more fundamental study of silicon diffusion and silicide formation in iron, which may be requisite for the semiconductor industry. Additionally, some analysis

of the volatile metal chlorides would be interesting and provide some insight as to how much chloride formation and vaporization actually occurs on these samples. It would also allow the user to characterize the metal chlorides to determine the exact species that is formed.

The testing system used in this work could also be used as a platform for future basic and applied research. One primary area of interest is the formation of carbide derived carbon. Often times, carbide derived carbon is formed from the reaction of silicon carbide with chlorine gas to form silicon tetrachloride and diamond like carbon. One large hurdle in this work is the handling and neutralization of the silicon tetrachloride product. The furnace system developed for chlorosilane corrosion testing could be repurposed for this research as it has been proven to handle and neutralize chlorosilanes properly.

POSTFACE

The work described in this dissertation represents the bulk of the independent research that the author performed during his time in the High Temperature Materials Laboratory at Montana State University. However, there was a significant amount of unpublishable or not yet publishable work that was completed that will be mentioned here. This work includes the development of thin film magnesium alloys for corrosion resistance, the management of several testing services contracts, and significant assistance in projects related to chromium evaporation and condensation.

Magnesium alloys are of significant interest to engineers due to their high strength to weight ratio. However, they oxidize very quickly, even at room temperature, rendering them useless for service. The objective of this research was to develop thin film magnesium alloys by co-depositing magnesium with iron, chromium, and/or titanium using a magnetron sputtering system. The study showed that passive films could be deposited using this technique, but they generally contained less than 50% magnesium. The results of this study were presented in a poster format at the 43rd International Conference on Metallurgical Coatings and Thin Films. At the present time, this project is ongoing with further characterization of the magnesium alloys scheduled. This may lead to publishable results in the future.

Chromium evaporation is problematic in many systems including fuel cells and car exhausts. The deposition of volatile chromium species can result in a trivalent or hexavalent condensed phase. Trivalent chromium may be problematic from a performance perspective, but it is not a significant health risk. However, hexavalent

chromium is a known toxin and it must be treated as hazardous if collected. Therefore, a collection technique should preferentially attract trivalent chromium rather than hexavalent chromium. This project focused on characterizing the chromium collected on fiber insulation that was vaporized from stainless steel at high temperatures in humid environments using a variety of surface and bulk analytical techniques. At the present time, this project is being directed by Greg Tatar, a fellow graduate student in the High Temperature Materials Laboratory. This work will likely lead to publication in the future.

Many of the experiments conducted for this dissertation were facilitated by testing services contracts. Testing services contracts are between the university and industry and allow the university to perform a test for industry and report back the results. The author's graduate experience included managing several testing services contracts that focused primarily on high temperature corrosion testing and surface analysis of proprietary materials. Industries typically made important materials decisions based on data the author collected and presented. While this lead to unpublishable work, it was invaluable due to the resources it provided and the experience with corrosion testing systems and surface analysis techniques. This work also included material and personnel management, industrial contacts, and industrial guidance; all essential parts of the author's graduate school experience.

REFERENCES CITED

[1] W.D. Callister, Materials Science And Engineering: An Introduction, John Wiley & Sons, 2007.

[2] J.C. Wadsworth, G; Hemley, R, Basic Research Needs for Materials under Extreme Environments, in, Department of Energy, 2008.

[3] I.H. Shames, Elastic And Inelastic Stress Analysis, Taylor & Francis, 1997.

[4] Y. Bar-Cohen, High Temperature Materials and Mechanisms, in, Bosa Roca : CRC Press, Bosa Roca, 2014.

[5] D.J. Young, High Temperature Oxidation and Corrosion of Metals, Elsevier, 2008.

[6] N. Birks, G.H. Meier, F.S. Pettit, Introduction to the High Temperature Oxidation of Metals, Cambridge University Press, 2006.

[7] M.F. Ashby, H. Shercliff, D. Cebon, Materials: Engineering, Science, Processing and Design, Elsevier Science, 2007.

[8] G. Lai, High-temperature corrosion: Issues in alloy selection, JOM, 43 (1991) 54-60.

[9] N. Birks, G.H. Meier, F.S. Pettit, Introduction to the High Temperature Oxidation of Metals, Cambridge University Press, 2009.

[10] W.M. Ingle, M.S. Peffley, Kinetics of the Hydrogenation of Silicon Tetrachloride, Journal of The Electrochemical Society, 132 (1985) 1236-1240.

[11] T.I. Kamins, Deformation Occurring during the Deposition of Polycrystalline-Silicon Films, Journal of The Electrochemical Society, 121 (1974) 681-684.

[12] S.F. Nitodas, S.V. Sotirchos, Development and Validation of a Mathematical Model for the Chemical Vapor Deposition of Silica from Mixtures of Chlorosilanes, Carbon Dioxide, and Hydrogen, Journal of The Electrochemical Society, 149 (2002) C120-C129.

[13] T.O. Sedgwick, Analysis of the Hydrogen Reduction of Silicon Tetrachloride Process on the Basis of a Quasi-Equilibrium Model, Journal of The Electrochemical Society, 111 (1964) 1381-1383.

[14] R.C. Jaeger, Introduction to Microelectronic Fabrication, Prentice Hall, 2002.

[15] G.B. Masson, Mary, 2015 Snapshot of Global Photovoltaic Markets, in, International Energy Agency, 2015.

[16] B.F. Hazeltine, Chad; Wenjun, Qin, Advancements in the commercial production of polysilicon, in, 2010.

[17] J.Y.P. Mui, CORROSION MECHANISM OF METALS AND ALLOYS IN THE SILICON-HYDROGEN-CHLOROSILANE SYSTEM AT 500 C, Corrosion, 41 (1985) 63-69.

[18] J.Y. Lee, W.H. Lee, Y.-K. Park, H.Y. Kim, N.Y. Kang, K.B. Yoon, W.C. Choi, O.B. Yang, Catalytic conversion of silicon tetrachloride to trichlorosilane for a poly-Si process, Solar Energy Materials and Solar Cells, 105 (2012) 142-147.

[19] J. Acker, K. Bohmhammel, Compensation effect in trichlorosilane synthesis, Journal of Organometallic Chemistry, 686 (2003) 151-157.

[20] D.M. Powell, R. Fu, K. Horowitz, P.A. Basore, M. Woodhouse, T. Buonassisi, The capital intensity of photovoltaics manufacturing: barrier to scale and opportunity for innovation, Energy & Environmental Science, 8 (2015) 3395-3408.

[21] P. Daniel, R. Rapp, Halogen Corrosion of Metals, in: M. Fontana, R. Staehle (Eds.) Advances in Corrosion Science and Technology, Springer US, 1976, pp. 55-172.

[22] F.M. d'Heurle, P. Gas, Kinetics of formation of silicides: A review, Journal of Materials Research, 1 (1986) 205-221.

[23] Y. Ihara, H. Ohgame, K. Sakiyama, K. Hashimoto, The corrosion behaviour of iron in hydrogen chloride gas and gas mixtures of hydrogen chloride and oxygen at high temperatures, Corrosion Science, 21 (1981) 805-817.

[24] N.S. Jacobson, Reaction of iron with hydrogen chloride-oxygen mixtures at 550°C, Oxid Met, 26 (1986) 157-169.

[25] Y. Sato, D. Young, High-Temperature Corrosion of Iron at 900°C in Atmospheres Containing HCl and H2O, Oxid Met, 55 (2001) 243-260.

[26] A.L. Cabrera, J.F. Kirner, Formation of silicon diffusion coatings on ferrous alloys from their reaction with silane, Surface and Coatings Technology, 39–40, Part 1 (1989) 43-51.

[27] A.L. Cabrera, J.F. Kirner, R. Pierantozzi, Si diffusion coating on steels by SiH4/H2 treatment for high temperature oxidation protection, Journal of Materials Research, 5 (1990) 74-82.

[28] M. Rebhan, R. Meier, A. Plagge, M. Rohwerder, M. Stratmann, High temperature chemical vapor deposition of silicon on Fe(100), Applied Surface Science, 178 (2001) 194-200.

[29] M. Rebhan, M. Rohwerder, M. Stratmann, CVD of silicon and silicides on iron, Applied Surface Science, 140 (1999) 99-105.

[30] C. Klam, J. Millet, H. Mazille, J. Gras, Chemical vapour deposition of silicon onto iron: influence of silicon vapour phase source on the composition and nature of the coating, Journal of Materials Science, 26 (1991) 4945-4952.

[31] N.R. Baldwin, D.G. Ivey, Iron silicide formation in bulk iron-silicon diffusion couples, Journal of Phase Equilibria, 16 (1995) 300-307.

[32] Y. Zhang, D.G. Ivey, Fe3Si formation in Fe–Si diffusion couples, Journal of Materials Science, 33 (1998) 3131-3135.

[33] Y. Ihara, H. Ohgame, K. Sakiyama, K. Hashimoto, The corrosion behaviour of nickel in hydrogen chloride gas and gas mixtures of hydrogen chloride and oxygen at high temperatures, Corrosion Science, 22 (1982) 901-912.

[34] B.J. Downey, J.C. Bermel, P.J. Zimmer, Kinetics of the Nickel-Chlorine Reaction at Temperatures Between 350 and 600 C, Corrosion, 25 (1969) 502-508.

[35] G.F. Iriarte, Growth of nickel silicide (NiSix) nanowires by silane decomposition, Current Applied Physics, 11 (2011) 82-86.

[36] Y. Ihara, H. Ohgame, K. Sakiyama, K. Hashimoto, The corrosion behaviour of chromium in hydrogen chloride gas and gas mixtures of hydrogen chloride and oxygen at high temperatures, Corrosion Science, 23 (1983) 167-181.

[37] E. D'Anna, G. Leggieri, A. Luches, G. Majni, G. Ottaviani, Chromium silicide formation under pulsed heat flow, Thin Solid Films, 136 (1986) 93-104.

[38] J. Acker, K. Bohmhammel, Reactivity of Intermetallic Compounds: A Solid State Approach to Direct Reactions of Silicon, The Journal of Physical Chemistry B, 106 (2002) 5105-5117.

[39] J. Acker, I. Röver, R. Otto, G. Roewer, K. Bohmhammel, Formation of transition metal silicides by solid–gas reactions: thermodynamic and kinetic considerations, Solid State Ionics, 141–142 (2001) 583-591.

[40] C.V.S.Y. Jain, O.P., Thermodynamics of n-alkane solutions: Part VIII - Vapour pressures & excess free energies for the SiCl4/n-hexane system, Indian Journal of Chemistry, (1973) 28-30.

[41] Y. Leng, Scanning Electron Microscopy, in: Materials Characterization, Wiley-VCH Verlag GmbH & Co. KGaA, 2013, pp. 127-161.

[42] Y. Leng, X-Ray Diffraction Methods, in: Materials Characterization, Wiley-VCH Verlag GmbH & Co. KGaA, 2013, pp. 47-82.

[43] J. Aller, K. Ellingwood, N. Jacobson, P. Gannon, High Temperature Chlorosilane Corrosion of AISI 316L, Journal of The Electrochemical Society, 163 (2016) C452-C458.

[44] J.L. Aller, K. Ellingwood, B. Clark, P.E. Gannon, The Time and Temperature Dependence of AISI 316L Corrosion in Chlorosilane Environments, ECS Transactions, 66 (2015) 41-51.

[45] J.L. Aller, P. White, J. Gum, B. Clark, P.E. Gannon, High-Temperature Corrosion of AISI 316L in Chlorosilane Environments at 550°C, ECS Transactions, 64 (2015) 161-171.

[46] J. Aller, R. Mason, K. Walls, G. Tatar, N. Jacobson, P. Gannon, High-Temperature (550–700°C) Chlorosilane Interactions with Iron, Journal of The Electrochemical Society, 163 (2016) C666-C674.

[47] E.A. Owen, E.L. Yates, XLI. Precision measurements of crystal parameters, The London, Edinburgh, and Dublin Philosophical Magazine and Journal of Science, 15 (1933) 472-488.

[48] F.A.B. Sidorenko, A.N.; Shubina, T.S.; Skripova, Ye.A.; Zelenin, L.P., Magnetic susceptibility of solid solutions of the monosilicides Fe Si - Co Si and Fe Si - Ni Si, Physics of Metals and Metallography, 28 (1969) 91-96.

[49] J. Waliszewski, L. Dobrzyński, A. Malinowski, D. Satuła, K. Szymański, W. Prandl, T. Brückel, O. Schärpf, Magnetic moment distribution in Fe3−xCrxSi alloys, Journal of Magnetism and Magnetic Materials, 132 (1994) 349-358.

[50] F. Huyan, R. Larker, P. Rubin, P. Hedström, Effect of Solute Silicon on the Lattice Parameter of Ferrite in Ductile Irons, ISIJ International, 54 (2014) 248-250.

[51] W.C. Leslie, The physical metallurgy of steels, Washington : Hempisphere Pub. Corp. New York : McGraw-Hill, Washington : New York, 1981.

[52] H. Nieswaag, J.W. Nijhof, Influence of Silicon on Bainite Transformation in Ductile Iron Relation to Mechanical Properties, MRS Proceedings, 34 (1984) 411.

[53] M.A. Krishtal, T.A. Sirenko, É.G. Titenskii, G.I. Naumov, Structure and properties of Fe−C−Si alloys, Metal Science and Heat Treatment, 12 (1970) 78-80.

[54] Z. Yu, Two new minerals gupeiite and xifengite in cosmic dusts from Yanshan, Yen K'uang Ts'e Shih, (1984) 231-238.

[55] P. Roberge, Handbook of Corrosion Engineering, Mcgraw-hill, 1999.

[56] O. Kubaschewski, Iron - Binary Phase Diagrams, Springer - Verlag, Berlin, Germany, 1982.

[57] I. Ohnuma, S. Abe, S. Shimenouchi, T. Omori, R. Kainuma, K. Ishida, Experimental and Thermodynamic Studies of the Fe–Si Binary System, ISIJ International, 52 (2012) 540-548.

[58] B. Sepiol, G. Vogl, Atomistic determination of diffusion mechanism on an ordered lattice, Physical Review Letters, 71 (1993) 731-734.

[59] A. Gude, H. Mehrer, Diffusion in the D03-type intermetallic phase Fe3Si, Philosophical Magazine A, 76 (1997) 1-29.

[60] S. Kipp, M. Zöllner, O. Ott, K.D. Becker, Reactivity and transport in the system Fe-Si, Solid State Ionics, 172 (2004) 407-412.

[61] W.W. Smeltzer, D.J. Young, Oxidation properties of transition metals, Progress in Solid State Chemistry, 10 (1975) 17-54.

[62] M. Maloney, M. McNallan, The effect of chlorine on the kinetics of oxidation of cobalt in environments containing 0.5 atmosphere of oxygen between 900 K and 1200 K, Metallurgical Transactions B, 16 (1985) 751-761.

[63] J. Aller, N. Swain, M. Baber, G. Tatar, N. Jacobson, P. Gannon, Influence of silicon on high-temperature (600 °C) chlorosilane interactions with iron, Solar Energy Materials and Solar Cells, 160 (2017) 410-417.

[64] C.W. Bale, P. Chartrand, S.A. Degterov, G. Eriksson, K. Hack, R. Ben Mahfoud, J. Melançon, A.D. Pelton, S. Petersen, FactSage thermochemical software and databases, Calphad, 26 (2002) 189-228.